

# Deep Near Infrared Mapping of Young and Old Stars in Blue Compact Dwarf Galaxies

Luz M. Cairós

luzma@uni-sw.gwdg.de

*Universitäts-Sternwarte Göttingen, Geismarlandstr. 11, 37083, Göttingen, Germany.  
Instituto de Astrofísica de Canarias, Vía Láctea, E-38200 La Laguna, Tenerife, Canary  
Islands, Spain. Departamento de Astronomía, Universidad de Chile, Casilla 36-D, Santiago  
de Chile, Chile*

Nicola Caon

ncaon@ll.iac.es

*Instituto de Astrofísica de Canarias, Vía Láctea, E-38200 La Laguna, Tenerife, Canary  
Islands, Spain*

Polychronis Papaderos

papade@uni-sw.gwdg.de

*Universitäts-Sternwarte Göttingen, Geismarlandstr. 11, 37083, Göttingen, Germany*

Kai Noeske

knoeske@uni-sw.gwdg.de

*Universitäts-Sternwarte Göttingen, Geismarlandstr. 11, 37083, Göttingen, Germany*

José M. Vílchez

jvm@iaa.es

*Instituto de Astrofísica de Andalucía, CSIC, Apdo. 3004, 18080 Granada, Spain*

Begoña García Lorenzo

bgarcia@ing.iac.es

*Isaac Newton Group of Telescopes, E-38780 Santa Cruz de La Palma, La Palma, Canary  
Islands, Spain*

Casiana Muñoz-Tuñón

cmt@ll<sup>1</sup>.iac.es

*Instituto de Astrofísica de Canarias, Vía Láctea, E-38200 La Laguna, Tenerife, Canary  
Islands, Spain*

## 1. Introduction

Blue Compact Dwarf (BCD) galaxies were first defined as compact and low-luminosity objects (starburst diameter  $\leq 1$  kpc;  $M_B \geq -18$  mag), with optical spectra similar to those presented by H II regions in spiral galaxies (Sargent & Searle 1970; Thuan & Martin 1981). Further work showed that they are metal-deficient galaxies — the oxygen abundance of their ionized gas varying between  $Z_\odot/50$  and  $Z_\odot/2$  — which form stars at a rate that would exhaust their gas content on a time scale much shorter than the age of the Universe. Nowadays it seems clear that among the galaxies originally classified as BCDs we find a wide range of luminosities ( $-12 \geq M_B \geq -21$  mag) and morphologies, the latter probably reflecting different evolutionary states and star formation histories (Loose & Thuan 1986; Noeske et al. 2000; Kunth & Östlin 2000; Cairós et al. 2001a, 2002; Bergvall & Östlin 2002). Initially it was hypothesized that BCDs are truly young galaxies, forming their first generation of stars (Sargent & Searle 1970; Lequeux & Viallefond 1980; Kunth & Sargent 1986; Kunth, Maurogordato, & Vigroux 1988); the subsequent detection of an extended, redder stellar host galaxy in the vast majority of them has revealed that most BCDs are old systems (Loose & Thuan 1986; Telles 1995; Papaderos et al. 1996a; Doublier et al. 1997; Doublier, Caulet, & Comte 1999; Cairós 2000; Cairós et al. 2001a,b; Bergvall & Östlin 2002) undergoing recurrent star-forming episodes (Thuan 1991; Mas-Hesse & Kunth 1999).

BCDs are attracting a great deal of interest in astrophysical research, as it has become clear that they could be the

touchstones for understanding several fundamental astrophysical problems. Even if most BCDs are not genuinely young systems, their gas-richness and metal-deficiency make them useful objects for constraining the primordial  $^4\text{He}$  abundance (Pagel et al. 1992; Masegosa, Moles, & Campos-Aguilar 1994; Thuan, Izotov, & Lipovetsky 1995; Izotov, Thuan, & Lipovetsky 1997; Izotov & Thuan 1999) and early metal enrichment in galaxies. Furthermore, BCDs are ideal laboratories for the study of many topics related to star formation (SF), by avoiding the complications of those mechanisms, such as density waves, that operate in spiral galaxies (O’Connell, Thuan, & Goldstein 1978; Thuan 1991; Brosch, Heller, & Almozno 1998). Last, it has been suggested that these systems could be the nearby counterparts of the faint blue galaxies detected at intermediate redshifts (Koo et al. 1994, 1995; Guzmán et al. 1996, 1997). Should this be the case, BCDs offer the possibility of studying the properties of this galaxy class with an accuracy and spatial resolution that cannot be achieved at larger distances.

In spite of the interest that these systems have attracted, the basic questions concerning their evolutionary status, formation history and mechanisms that trigger their star-forming activity are still open. In particular, the assessment of the properties of the stellar low-surface-brightness component (LSBC) underlying the starburst regions in BCDs is a fundamental task. This older component hosts most of the galaxy’s stellar mass. Provided that Dark Matter (DM) does not dominate the mass within the Holmberg

radius (Papaderos et al. 1996b), the stellar LSBC is, together with the H I halo, mainly responsible for the global gravitational potential within which the starburst phenomenon takes place. Moreover, deep spectrophotometric studies of the LSBC are indispensable for putting constraints on the evolutionary status and the formation history of BCDs. The comparison of the properties of the LSBC (e.g., structural parameters, average colors and color gradients) with those of other dwarf galaxy classes: dwarf irregulars (dIIs), dwarf ellipticals (dEs), and low surface brightness (LSB) galaxies, will be crucial to test evolutionary scenarios that link those galaxies with BCDs (Thuan 1985; Davies & Phillipps 1988; Papaderos et al. 1996b; Marlowe et al. 1997; Marlowe, Meurer, & Heckman 1999; Cairós 2000), or connect the different morphological subclasses of BCDs (Noeske et al. 2000).

A precise determination of the structural properties of the LSBC is also necessary for an elaborate study of the star-forming regions of BCDs (Telles 1995; Vanzi et al. 1996; Telles & Terlevich 1997; Cairós 2000; Gil de Paz et al. 2000; Doublier, Caulet, & Comte 2001; Vanzi, Hunt, & Thuan 2002; Papaderos et al. 2002). Recently Cairós et al. (2002) have compared the photometric parameters of the individual star-forming knots in the BCD Mrk 370 before and after subtracting the contribution from the older stars, and found significant differences in the results (the LSBC contribution typically shifts the starburst colors by 0.2–0.4 mag). Evidently such a correction must be computed and applied before using the colors of the starburst knots to estimate their age.

The present study constitutes the third part of an extensive multiwavelength investigation of nearby BCDs. In the first stage of this program (Paper I) optical broadband images of 28 BCDs were used to examine the optical morphology and study the photometric structure of these systems by means of deep surface photometry. In Paper II we provided integrated photometry of the galaxies and produced an atlas of detailed color and H $\alpha$  maps.

From the latter study it was concluded that the structural parameters and the evolutionary status of the stellar population underlying the starburst component can not be determined from optical information alone. The optical domain is strongly affected by interstellar reddening, and dominated by the emission of young stars and ionized gas all over the inner part of a BCD. Moreover, optical colors are not sensitive age indicators for stellar populations several Gyr old. For instance, for a single stellar population, the  $B-V$  and  $V-R$  colors increase by only  $\approx 0.1$  mag when the age varies from 5 to 15 Gyrs (see, e.g., Vazdekis et al. 1996). The NIR spectral window which traces primarily the old stellar populations would be best suited for studies focusing on the LSBC. It offers the following advantages over the optical: i) the contribution of young stars and nebular emission lines to the total light of the galaxy is smaller than in the optical. The models by Krüger, Fritze-v. Alvensleben, & Loose (1995) predict that a moderately strong burst at its peak in luminosity accounts for only  $\approx 20\%$  of a BCD's emission in the  $K$ -band, compared to  $\geq 80\%$  in  $B$ . Dealing with the BCD II Zw 40, Vanzi et al. (1996) found that approximately one

half of the total  $B$  and  $V$  emission of the star-forming regions comes from emission lines, whereas the latter contribute to less than 10% in the  $H$  and  $K$  bands. There is also observational evidence that the starburst fades away at galactocentric distances smaller than in the optical (Alton et al. 1994; James 1994; Vanzi et al. 1996; Beck, Kelly, & Lacy 1997). ii) NIR broad-band colors are much less affected by interstellar extinction, the extinction in  $H$  being a factor of  $\sim 6$  lower than in  $V$ . iii) A combination of optical-NIR colors allow, in principle, to distinguish among more or less evolved populations of old stars (Thuan 1985; Östlin 1998; Peletier, Valentijn, & Jameson 1990; Peletier et al. 1999).

Consequently, the next stage in our project has been to extend our analysis to the NIR regime. Here we report on deep surface brightness photometry in  $J$ ,  $H$  and  $K_s$  for a sample of 9 BCD galaxies, 8 of which have been previously analyzed by us in the optical (see Papers I and II).

## 2. Observations, Data Reduction and Flux Calibration

### 2.1. Observations

The basic data for the sample galaxies are given in Table 1. Column 5 lists the galaxies distances, which were computed assuming a Hubble flow, with a Hubble constant  $H_0 = 75 \text{ km s}^{-1} \text{ Mpc}^{-1}$ , after correcting recession velocities relative to the centroid of the local group for virgocentric infall. Column 6 lists the absorption coefficient in the  $B$  band. Absolute magnitudes (column 7) have been obtained from the  $B$  asymptotic magnitudes (Cairós 2000), us-

ing the distances tabulated in column 5. The  $B$  magnitude of Mrk 407 has been obtained from NED.

NIR imaging of the galaxies in  $J$ ,  $H$  and  $K_s$  was obtained in April 2000 at the 4.2m William Herschel Telescope (WHT, Observatorio del Roque de los Muchachos, ORM, La Palma) during three consecutive nights. We used the infrared camera INGRID (Isaac Newton Group Red Imaging Device), equipped with a  $1024 \times 1024$  pixel Hawaii detector array. The scale was  $0''.242 \text{ pixel}^{-1}$  and the field of view was  $4'.13 \times 4'.13$ . We preferred to use the  $K_s$  instead of the standard  $K$  filter, as the former has a more favorable transmission curve, which cuts off more efficiently the thermal emission from the telescope and the atmosphere, thus reducing considerably the background noise in the final images. Throughout this work we adopt  $K = K_s$ , which turns out to be a reasonable assumption (Persson et al. 1998; González-Pérez, Kidger, & Martin-Luis 2001).

During the first two nights of the run the seeing was quite stable, varying between  $0''.8$  and  $1''.2$  FWHM, while during the third night it deteriorated to values between  $1''$  and  $1''.8$ .

The galaxies Mrk 36, II Zw 70, II Zw 71 and Mrk 297 were also observed in April 1999 at the Centro Astronómico Hispano Alemán (CAHA) at Calar Alto with the  $1024 \times 1024$  pixel OMEGA PRIME camera, mounted at the 3.5m telescope. The scale was  $0''.3961 \text{ pixel}^{-1}$ , and the total field of view  $6'.76 \times 6'.76$ . The targets were imaged in the  $J$ ,  $H$  and  $K_m$  bands ( $K_m$  is, like  $K_s$ , a modified  $K$  filter that reduces the thermal background; Wainscoat & Cowie 1992). The seeing varied between  $1''.2$  and

2'' FWHM. A complete log of the observations is provided in Table 2.

## 2.2. Data Reduction

The high sky background levels in the NIR (especially in  $H$ , because of OH air-glow and in  $K$ , because of thermal emission from sky, telescope and dome) make the observing strategy and the data reduction process more complicated than when observing in the optical. The telescope must chop between on-target and off-target positions to properly sample variations of the sky-background. Additionally, the total integration time spent at each of these positions must be split into many sub-exposures of a few seconds each in order not to exceed the linearity range of the detector.

The individual exposure times in INGRID were typically 50 s in  $J$ , 40 s in  $H$  and 15 s in  $K_s$ , with sets of 2–4 exposures taken at each position. The total on-target integration times are listed in Table 2. For the CAHA observations, the telescope position was changed between pointings of 60 s each, which were split up into sub-exposures of 6, 3 and 2 s in  $J$ ,  $H$  and  $K_m$ , respectively.

The processing and calibration of the frames was performed using standard procedures available in IRAF<sup>1</sup>.

We first built a bad pixel mask, which was applied to every raw frame. This mask is used to correct for bad pixels by interpo-

lating the flux level along neighboring lines and columns. Second, the sky background has to be subtracted from each frame. A typical NIR frame contains flux contributions from the target, from the sky background, from the warm telescope and from dome scattered light. Hence, it is necessary to take sky frames to measure and remove these contributions, which may fluctuate on time-scales of minutes. Depending on the size of the target, we have employed two different procedures in order to sample the background: 1) when dealing with small objects (optical diameter  $\leq 30''$ ), we offset the telescope between exposures, producing a sequence in which the target is placed on different sections (typically the four quadrants) of the array. The median average of these frames will then provide a clean sky frame (free from the target, cosmic rays and point-like sources). This procedure has the benefit that all observing time is spent on the target. 2) The above technique cannot be used when observing large objects which extend over a significant portion of the detector. In those cases, in order to obtain a clear patch of sky, we offset the telescope some arcmin from the target position, each time dithering by several arcsecs.

Afterwards, the sky subtracted frames must be flat-fielded. To create a proper flat-field, which contains only information on the overall response and pixel-to-pixel sensitivity variations of the telescope/camera combination, two type of flat-field images are needed: the "flat on", with a high count level, and the "flat off", with the same duration of the "on" but with a low count level. In the INGRID run, flats were taken during twilight ("flat

---

<sup>1</sup>IRAF (Image Reduction and Analysis Facility) is distributed by the National Optical Astronomy Observatories, operated by the Association of Universities for Research in Astronomy, Inc., under cooperative agreement with the National Science Foundation.

TABLE 1  
SAMPLE OF GALAXIES

Galaxy	Other designations	R.A. (2000)	Dec.	D (Mpc)	$A_B$ (mag)	$M_B$ (mag)
Mrk 407		09 47 47.6	39 05 04	23.2	0.069	-16.33
Mrk 33	Haro 2, Arp 233	10 32 31.9	54 24 03	22.3	0.052	-18.28
Mrk 35	Haro 3, NGC 3353	10 45 22.4	55 57 37	15.6	0.031	-17.75
Mrk 36	Haro 4	11 04 58.5	29 08 22	10.3	0.131	-14.69
UM 462	Mrk 1307	11 52 37.3	-02 28 10	14.0	0.083	-16.07
II Zw 70	Mrk 829	14 50 56.5	35 34 18	19.0	0.053	-16.55
II Zw 71		14 51 14.4	35 32 31	19.6	0.055	-17.00
I Zw 123	Mrk 487	15 37 04.2	55 15 48	12.5	0.062	-15.04
Mrk 297	NGC 6052, Arp 209	16 05 12.9	20 32 32	65.1	0.330	-21.01

TABLE 2  
LOG OF THE OBSERVATIONS

Galaxy	Date	Telescope	Exposure time (s)		
			$J$	$H$	$K_s$
Mrk 407	Apr. 00	WHT 4.2m	1200	1600	2205
Mrk 33	Apr. 00	WHT 4.2m	1700	1200	2565
Mrk 35	Apr. 00	WHT 4.2m	800	720	1440
Mrk 36	Apr. 00	WHT 4.2m	1200	240	120
	Apr. 99	CAHA 3.5m	...	1500	2250
UM 462	Apr. 00	WHT 4.2m	1200	1280	1800
II Zw 70	Apr. 00	WHT 4.2m	1700	640	540
	Apr. 99	CAHA 3.5m	2280	420	990
II Zw 71	Apr. 00	WHT 4.2m	960	720	480
	Apr. 99	CAHA 3.5m	1080	360	1320
I Zw 123	Apr. 00	WHT 4.2m	1300	1600	1440
Mrk 297	Apr. 00	WHT 4.2m	600	420	360
		CAHA 3.5m	...	1200	600

on” when the sky was still bright, “flat off” when the sky was darker). In the CAHA run, the flat-fields were obtained by taking exposures of the dome with the lamps on and off. The subtraction of the dark flat from the bright one (after averaging out the several individual frames) removes the dome, telescope and dark-current contributions, giving the final flat-field image.

The sky-subtracted target frame is then divided by the flat-field and, finally, all frames in the same band are aligned, brought to the same resolution by convolution with a gaussian of appropriate width, and combined.

In the case of II Zw 70 and II Zw 71, we built the final frames by combination of the images taken at CAHA and at the WHT. The WHT images were resampled and convolved by a gaussian to match the same pixel size and actual resolution of the CAHA frames; finally they were averaged weighting them by their signal-to-noise ratio.

### 2.3. Flux Calibration

Flux calibration was done through the observation of photometric standard stars selected from the UKIRT list of faint IR standard stars. The stars FS 17, FS 21, FS 27 and FS 35 were observed throughout each night at different airmasses. The range of colors in the NIR is very small for normal stars (particularly  $H-K$ ) and, as a consequence, accurate determination of the color term could not be achieved using the standard list. Thus, when calculating the calibration constant and the magnitudes of the galaxies, we neglect the color term and resolve the following equation:

$$m_{\lambda_0} = m_{\lambda_i} + a_0 + a_1 X, \quad (1)$$

where  $m_{\lambda_0}$  is the magnitude in the standard system,  $m_{\lambda_i}$  is the instrumental magnitude,  $X$  is the airmass at which the observations were done and  $a_i$  are the calibration constants to be determined.

The observations taken at CAHA were calibrated using the INGRID frames by matching the fluxes computed within a sequence of centered apertures. The magnitudes in  $K_s$  and  $K_m$  were transformed following Wainscoat & Cowie (1992). Note that the  $H$  and  $K_s$  INGRID images of Mrk 36 and Mrk 297 were used only to calibrate the CAHA exposures.

## 3. Photometry and Morphology of the Galaxies

### 3.1. Isophotal magnitudes

In order to allow a direct comparison of our photometry with values derived in other studies, we list in Table 3 the isophotal magnitudes of the sample BCDs in  $J$ ,  $H$  and  $K_s$ , as respectively determined within the 23, 22 and 21 mag arcsec<sup>-2</sup> isophote. These magnitudes are tabulated alongside with the uncertainties resulting from the zero-point calibration and the subtraction of the sky background.

Integrated magnitudes were corrected for Galactic extinction by using the absorption coefficient in the  $B$  band ( $A_B$ ) and the color excess  $E(B-V)$  derived from Schlegel, Finkbeiner, & Davis (1998). The absorption coefficients in the NIR bands ( $A_J$ ,  $A_H$  and  $A_K$ ) are derived by assuming the standard extinction law ( $R_V = A_V/E(B-V) = 3.1$ ), and using the  $A_\lambda$  curve from Cardelli, Clayton, & Mathis

(1989). The values of  $A_J$  for each object are also listed in Table 3.

### 3.2. Contour and Color Maps

Figure 1 (top panel, on the left) show the  $J$  band contour maps of the sample galaxies ( $H$  band for Mrk 297). In order to better trace the lower surface brightness levels, the outer contours were computed after smoothing the original image by a boxcar sliding average, with a window size increasing with the distance to the center (typically up to  $7 \times 7$  or  $9 \times 9$  pixels).

We find that the morphology of the galaxies is usually very similar in the optical and in the NIR (see the atlas of  $B$  band contour maps in Paper I). Because of the better spatial resolution in the NIR, in several cases (UM 462 being the most striking) we can resolve knots of SF which appeared blurred in the optical frames. Also, because our NIR data do not reach surface brightness levels as deep as in the optical, some galaxies (for instance, Mrk 36 and UM 462), appear slightly irregular in their outer part.

Using the NIR images, we grouped the galaxies into the four different morphological classes defined in Paper II and confirm in all cases the classification previously made on optical frames.

We have also computed optical-NIR color maps of our sample BCDs. These maps were built after the calibrated frames have been aligned, brought to the same pixel scale (the one in the frames with the poorer resolution) and, finally, seeing-adapted. Usually the optical-NIR color maps are limited by the noise in the NIR frames, which is considerably higher than in the optical, so reliable information can

be only derived for the central, high intensity galaxy regions.

The  $V-K$  color maps of the galaxies ( $B-K$  in the case of II Zw 71) are displayed for the galaxies with the most interesting morphology in Figures 5 to 9. Extended dust patches are clearly visible in three galaxies: Mrk 33, Mrk 35 and Mrk 297.

### 3.3. Surface brightness, color and shape profiles

Figure 1 display the surface brightness profiles (SBPs) of the galaxies in the three NIR bands. We also present the numerical ellipticity and position angle distribution in the  $J$  band as a function of the equivalent radius  $R$ , as well as color profiles (CPs) in the NIR. Whenever optical information is available, we also computed optical-NIR CPs.

SBPs were built following the methods described in Cairós (2000) and in Paper I, which we summarize here. In the inner, irregular starburst regions, where the standard technique of fitting ellipses to the isophotes can not be applied, we used an alternative method, which does not require any assumption on the morphology of the object. We define  $A_n$  as the sum of the areas of all those pixels the intensity of which is higher than  $I_n$ :

$$A_n = N_{\text{pix},n} A_{\text{pix}}, \quad (2)$$

$N_{\text{pix},n}$  is the number of the pixels with  $I \geq I_n$  and  $A_{\text{pix}}$  is the pixel area in square arcseconds.

The flux  $F_0, F_1, \dots, F_n$  enclosed by the isophotes with intensities  $I_0, I_1, \dots, I_n$  (spaced 0.1 mag apart), enclosing areas



TABLE 3  
ISOPHOTAL MAGNITUDES

Galaxy	$A_J$ (mag)	$J$ (mag)	$H$ (mag)	$K_s$ (mag)
Mrk 407	0.014	$13.28 \pm 0.04$	$13.03 \pm 0.04$	$12.66 \pm 0.05$
Mrk 33	0.011	$11.28 \pm 0.02$	$10.84 \pm 0.03$	$10.65 \pm 0.04$
Mrk 35	0.006	$11.31 \pm 0.03$	$10.83 \pm 0.02$	$10.43 \pm 0.03$
Mrk 36	0.027	$14.29 \pm 0.03$	$14.03 \pm 0.03$	$13.95 \pm 0.04$
UM 462	0.017	$13.32 \pm 0.03$	$12.87 \pm 0.02$	$12.72 \pm 0.03$
II Zw 70	0.011	$13.42 \pm 0.05$	$13.05 \pm 0.04$	$13.00 \pm 0.05$
II Zw 71	0.012	$12.62 \pm 0.06$	$12.14 \pm 0.03$	$12.16 \pm 0.05$
I Zw 123	0.012	$13.76 \pm 0.02$	$13.25 \pm 0.03$	$13.20 \pm 0.04$
Mrk 297	0.069	$11.37 \pm 0.02$	$10.92 \pm 0.06$	$10.58 \pm 0.06$

NOTE.—Column 2: Galactic extinction in  $J$ ; (3)–(5): isophotal magnitudes in the different bands (within  $23 \text{ mag}/\square''$  in  $J$ ,  $22 \text{ mag}/\square''$  in  $H$  and  $21 \text{ mag}/\square''$  in  $K_s$ ), corrected for galactic extinction.

$A_0, A_1, \dots, A_n$ , is then calculated by performing consecutive integrations over the image. To each annulus we associate a radius  $R_n$ , equal to the radius of the circle whose area is the average of  $A_n$  and  $A_{n+1}$ :

$$R_n = ((A_n + A_{n+1})/2\pi)^{1/2}, \quad (3)$$

while the surface brightness  $\mu_n$  ( $\text{mag}/\square''$ ) is obtained by dividing the flux within each annulus by its area:

$$\mu_n = -2.5 \log[(F_{n+1} - F_n)/(A_{n+1} - A_n)] + \text{const}, \quad (4)$$

where const is the calibration constant. The surface brightness is then plotted versus the equivalent radius. Outside the starburst-dominated regions, our sample BCDs present a relatively regular and symmetric morphology. We derived the luminosity and geometrical profiles by fitting

ellipses to the isophotes, using the IRAF task *ellipse*. First we masked out foreground stars, smaller knots, and other disturbances. Then we ran the task on the original image and on images obtained by smoothing the former by a median average (with window sizes up to  $11 \times 11$  pixels), to improve the stability and reliability of the results in the outer galaxian regions.

The final surface brightness and geometrical profiles were then built by combining the profiles derived from the un-smoothed image in the inner parts with those derived from the smoothed images in the outer parts, checking that the profiles match well in the overlapping radial ranges.

The errors of the surface brightness levels are computed as the quadratic sum, in intensity, of the uncertainties given by the ellipse fitting algorithm and those in the sky subtraction. The latter (which is

not to be confused with the noise of the sky), is an estimate of how much the sky level varies around the galaxy as a result of large- or intermediate-scale residual gradients in the sky background, imperfect flat-fielding, etc.

Color profiles have been derived by subtracting the SBPs in the two bands, after the SBPs have been brought to the same resolution using gaussian smoothing and resampled to equal radial step. We note that in their very center CPs can still present sudden variations, as the SBP extraction technique employed at high-surface brightness levels where multiple star-forming knots are present does not allow to perfectly reproduce the color variations from knot to knot. In such areas two irregular "annuli" having the same equivalent radius in the two bands may have different shapes, so we might compare the signal from physically different spatial regions. Thus color profiles are only plotted outside the central 1–2".

We have found that, in agreement with the optical results, one can usually distinguish on near-infrared SBPs two components: the starburst and the LSBC host galaxy. This was found to be the case for 8 out of the 9 sample BCDs. Only in Mrk 407 we cannot separate the two components. However, given the faintness and compactness of the galaxy, we can neither prove nor rule out the presence of a LSBC; profiles reaching deeper surface brightness levels are clearly necessary to give a firm answer.

In all cases the SBPs have the same shape as the optical profiles (see Figure 1 in Paper I); however, the contribution of the starburst in the NIR is much less im-

portant than in the optical: the intensity peaks are less pronounced and the emission appears to be less extended (see also Noeske et al. 2003). For UM 462 the NIR profiles are, in their inner part, markedly steeper than the optical SBPs presented in Paper I, because of the much better resolution of the NIR data.

#### 4. Structure and colors of the underlying host

Surface photometry studies in the optical have clearly shown that the SBP of BCDs is the superposition of at least two components: the starburst, made up of the emission from young massive stars and from ionized gas, which dominates the light at high and intermediate intensity levels, and the stellar low surface brightness component, which dominates at larger radii and contains most of the system's stellar mass (Loose & Thuan 1986; Telles 1995; Papaderos et al. 1996a; Marlowe et al. 1997; Doublier et al. 1997; Östlin 1998; Doublier, Caulet, & Comte 1999; Cairós et al. 2001a,b; Bergvall & Östlin 2002).

However, not much in-depth work has been done so far on the properties of the LSBC, mainly because of two reasons: first, only recently it has been recognized that its structural properties may significantly influence the global star formation process in BCDs (Papaderos et al. 1996b; Cairós et al. 2002) and that its morphology may hold clues to their evolutionary state (Östlin, Bergvall, & Rönnback 1998; Doublier et al. 1997; Doublier, Caulet, & Comte 1999; Noeske et al. 2000; Kunth & Östlin 2000; Cairós et al. 2002); second, because of its faintness, a quantitative study of the LSBC (derivation of, e.g.,

scale lengths, total luminosities or color gradients) requires a great deal of observational and analysis effort.

The purpose of this section is to derive the NIR structural parameters of the LSB for the observed galaxies. The proper determination of these parameters requires some caution. In fact, in BCDs the emission from the young stars and the ionized gas camouflages the LSB at high and intermediate intensity levels; it is, therefore, fundamental to identify and measure the size of the region contaminated by the starburst, and derive the structural parameters of the LSB *outside* this region. Since this means to perform the fit usually for  $\mu_B \geq 24$  mag arcsec<sup>-2</sup> (Papaderos et al. 1996a; Bergvall & Östlin 2002, Paper I), it is essential to achieve deep surface brightness limits: the deeper the data, the larger the portion of the host galaxy that we can analyze, and therefore the more reliable the final results. In particular, three are the main requirements:

a) *Proper determination of the fit radial range.* Selecting the radial range of the SBP in which the fit is to be done is possibly the most critical point: we must make sure that we fit uniquely those regions of the galaxy free from starburst emission. In order to delimit this region, we took advantage of our optical data. By inspecting the optical color maps and H $\alpha$  images of the galaxies (Paper II), we defined an  $R_{\text{transition}}$  outside which the starburst emission is practically absent. The fit was then done in the interval  $R > R_{\text{transition}}$ . We notice that an examination of the SBP itself is not sufficient: in fact, the SBP might show no discontinuity or marked change of slope around  $R_{\text{transition}}$ , and one may be

tempted to extend inwards the fit interval, which makes the derived LSB structural parameters significantly skewed by the inclusion of starburst light.

b) *Deep and extended surface brightness profiles.* To fulfill it, we observed at 4m class telescopes with long exposures times, and did a careful flat-field correction and sky background subtraction, both crucial steps in order to reach the required surface brightness levels (27-28 mag/□" in  $B$ , 24-25 mag/□" in  $J$ ).

c) *Use of a suitable analytical model for the light distribution of the host.* A third important point is the choice of the most appropriate formula to describe the SBP of the host. So far, it has been common practice to adopt the exponential model. However, it is nowadays recognized that several LSB host have profiles that show systematic deviations from the exponential model. Here, we go further and explore the applicability of the Sérsic law in parametrizing the radial intensity distribution of the underlying LSB of BCDs.

Underlooking or underestimating the importance of the above points can lead to incorrect determinations of the LSB structural parameters, and may explain the large discrepancies among the results obtained in the optical bands by different authors (see the discussion in Kunth & Östlin 2000; Cairós 2000; Cairós et al. 2001a).

#### 4.1. Exponential and Sérsic models

So far, it has been common practice to model the host galaxy of BCDs by fitting an exponential function to the outer parts of SBPs (Telles 1995; Papaderos et al. 1996a; Marlowe et al. 1997; Östlin 1998;

Cairós et al. 2001a).

$$I(R) = I_0 \exp(-R/\alpha), \quad (5)$$

where  $I_0$  is the central intensity and  $\alpha$  is the scale length. Equation 5 corresponds to a straight line in the  $R - \mu$  diagram. Its total magnitude,  $m_T$ , is then given by:  $m_T = \mu_0 - 5 \log(\alpha) - 1.995$ . However, it is clear that several SBPs show a curvature in the  $R - \mu$  diagram and, thus, the derived exponential fit parameters may depend on the radial range where the fit is done (see, for instance, the SBP of Mrk 370 and Mrk 33, Figure 2, Paper I). Cairós (2000) has observed a concave outer slope in several deep optical SBPs, and remarked that in those cases, a seemingly irreproachable exponential fit to the LSB emission could just be due to fitting a small portion of the SBP. Conversely, in some BCDs an inwards extrapolation of the exponential slope of the LSB implies for intermediate to small radii an intensity higher than the observed value. This fact, which is suggestive of an overall convex LSB profile, has been discussed in, e.g., Papaderos et al. (1996a); these authors (see also Noeske et al. 2003) proposed a modified exponential distribution flattening in its inner part to fit SBPs presenting the above mentioned characteristics.

In the last years, the Sérsic law has grown in popularity as the most appropriate description of the SBP of ellipticals and bulges:

$$I(r) = I_e \exp(-b_n[(r/r_e)^{1/n} - 1]), \quad (6)$$

The coefficient  $b_n$  is chosen so that  $r_e$  is the radius enclosing half of the total light

of the model and  $I_e$  denotes the intensity at  $r_e$ . The above formula includes as particular cases the exponential ( $n = 1$ ) and the de Vaucouleurs ( $n = 4$ ) laws. Caon, Cappacioli, & D’Onofrio (1993) showed that the  $n$  parameter is directly correlated to the size/luminosity of elliptical galaxies. This finding has been extended to brightest cluster members (Graham et al. 1996), bulges of spirals (Andredakis, Peletier, & Balcells 1995) and dwarf ellipticals (Young & Currie 1994). A physical interpretation of the shape parameter  $n$  has been proposed by Trujillo, Graham, & Caon (2001), in the sense that a larger  $n$  corresponds to a higher central light (and possibly mass) concentration. Notably, the light concentration also correlates with the central stellar velocity dispersion  $\sigma$  and with the mass of the central super-massive black-hole (Graham et al. 2001).

It is then natural to ask whether the LSB in BCDs can be described by a Sérsic law too, and whether the index  $n$  correlates with other properties of the LSB, such as total luminosity, scale length or central surface brightness. Here we study the shape of NIR profiles in their outer regions, by fitting a Sérsic law. We also investigate how the resulting model parameters may be influenced by the precise radial range in which the profile is fitted and by errors in the sky subtraction.

#### 4.2. On fitting a Sérsic law to the SBP of the underlying host galaxy

As we shall demonstrate below, fitting Sérsic models to the LSB emission in BCDs is not as straightforward as one may think, and the result may be entirely dic-

tated by observational uncertainties. For the determination of  $n$  for a real SBP to be reliable, the fitting range must be quite extended, spanning a surface brightness interval of at least 4 magnitudes. This is not a problem when monocomponent galaxies are fitted, or when careful bulge-disk decomposition is done in deep images<sup>2</sup>. However, these requirements can hardly be met in BCD galaxies, where, as remarked earlier, the emission from the old stellar population in the central regions is overwhelmed by the starburst. For instance, in the  $B$  band the starburst emission affects the SBPs down to typically  $\mu_B \gtrsim 24$  mag arcsec<sup>-2</sup> (Papaderos et al. 1996a, Paper I), thus leaving only a range of at most 3 or 4 magnitudes on which to fit a Sérsic model to the outer part of a SBP. At these faint surface brightness levels, minor uncertainties in the sky subtraction or image flat-fielding can distort the SBP shape and strongly bias the derived parameters of Eq. 6.

Also, the Sérsic parameter  $n$  is poorly constrained when the fit is done on such limited surface brightness intervals (see Makino, Akiyama, & Sugimoto 1990). Small variations in the fitted radial range, and the inclusion or exclusion of a few datapoints may change the resulting  $n$  more than one would naively expect. In principle, the situation in the NIR domain should be more favorable, because the starburst contaminates the light to a lesser degree. However, because of the high sky background, the S/N ratio in the NIR data is lower than in the optical (especially in

<sup>2</sup>For instance, in Caon, Capaccioli, & D’Onofrio (1993) the typical range in surface brightness was 5–6 mag.

$K$ ), so it is very difficult to obtain SBPs as deep and extended as in the optical bands.

Because in several cases the BCD’s profiles show a relatively smooth curvature over a large radius range, one is tempted to enlarge the fit interval by decreasing  $R_{\text{transition}}$ , at the risk of including regions still affected by starburst light. In those cases the rms (the average scatter of the residuals between observations and fit) is merely a poor indicator for the validity of the fit solution, as it may marginally vary despite huge variations in the derived  $n$ . The steeply increasing flux contribution of the starburst towards small radii can indeed mimic a Sérsic profile with a higher  $n$  ( $> 4$ , see, e.g. the discussion in Papaderos et al. 1996a).

#### 4.2.1. Illustrative examples: Mrk 33 and Mrk 35

In order to illustrate the above problems, and provide some quantitative estimates of how they could affect the derived Sérsic parameters, we carry out a series of fits to the LSBC light profile of the BCDs Mrk 33 and Mrk 35. For both we have deep, good quality data. Mrk 33 exhibits a smooth intensity decay over its whole radius range, so that one may be tempted to fit its SBP using a single Sérsic law. The  $R_{\text{transition}}$  of this system can only be inferred from color or H $\alpha$  maps, i.e. cannot be read off its SBP. On the other hand, in Mrk 35  $R_{\text{transition}}$  is approximately equal to the radius where a sharp change in the SBP slope occurs, outside which the LSBC shows an exponential behavior.

A typical approach to assess the uncertainties on the parameters obtained from fitting models to galaxy light profiles is to

create first a 2-D galaxy images based on the selected analytical formula. From it, a number of simulations are built by adding noise, convolving by seeing, over or under-subtracting the sky background, etc., and the light profile is then extracted and fitted; the difference between measured and input parameters is recorded. From the distribution of these differences the parameter uncertainty is then estimated. By repeating the above procedure for many combinations of input parameters, their uncertainties can be studied as function of, for instance, the total galaxy magnitude, or effective radius, or profile shape, etc.

However in the reality there are further and somewhat more complex source of uncertainties often neglected in the above scheme, so that these uncertainties may be actually under-estimated. For instance, the galaxy profile may be contaminated by small knots or other disturbances not adequately masked out before the ellipse fitting algorithm is run, or may be distorted by the presence of nearby bright stars. Also, the sky background may be inhomogeneous, presenting fluctuations on scales of the order of the galaxy size.<sup>3</sup>

So in the present paper we use our observed data to carry out a more realistic analysis of parameter uncertainties, based on comparing the parameters obtained from images taken in different bands and by fitting in different radial intervals.

---

<sup>3</sup>For our data, seeing is not that important, as  $R_{\text{transition}}$  is generally larger than the region affected by seeing convolution.

### *Dependence on the radial range*

We fitted a Sérsic law to the SBP of Mrk 33 and Mrk 35 in different radial intervals; in these and all subsequent fits, we assigned the same weight to all datapoints. This is to avoid that only a few points in the higher surface brightness portion of the profile dominate the fit, which could be almost insensitive to the outermost profile datapoints.

The Sérsic parameters thus obtained are summarized in Table 4.

- **Mrk 33** — Optical studies (Paper I) show that starburst emission is limited to the central  $16''$ , so the  $J$  band SBP can be safely fitted in the range  $20'' < R < 50''$ ,  $50''$  being the last observed datapoint; the fitting range corresponds to a surface brightness interval of  $\Delta\mu = 2.4$  mag. Fitting Eq. 6 gives  $n = 2.09$  with  $\text{rms} = 0.041$ . The smoothness and nearly constant curvature of the profile tempts to enlarge the fitted interval by extending it inwards to  $R = 10''$  ( $\Delta\mu \sim 4$  mag); this gives  $n = 4.07$  and an improved  $\text{rms} = 0.038$ . As evident from comparison of rows 3 and 4 in Table 4, the exclusion of one single datapoint from the fit can change  $n$  by nearly a factor of two.

A similar behavior is found when fitting Eq. 6 to the  $K_s$  band profile using the same starting radius (the  $K_s$  profile is less extended). In this case we obtain  $n = 1.29$  ( $\Delta\mu = 1.6$  mag,  $\text{rms} = 0.048$ ), fitting from  $R = 20''.20$ , and  $n = 5.98$  fitting from  $R = 10''.48$ , with only a very small

TABLE 4  
SÉRSIC PARAMETERS FOR MRK 33 AND MRK 35 AS FUNCTION OF THE RADIAL RANGE

Fit ID	Galaxy	Band	Radial range arcsec	Surface brightness range mag/□''	$n$	rms mag	$r_e$ arcsec	$\mu_e$ mag/□''	$m_{\text{LSBC}}$ mag
(1)	Mrk 33	$J$	20.47–49.90	21.23–23.68	2.09	0.041	17.76	20.99	11.68
(2)			10.25–49.90	19.71–23.68	4.07	0.038	11.87	20.03	11.26
(3)			21.29–39.12	21.40–22.91	3.73	0.030	15.41	20.67	11.38
(4)			20.47–39.12	21.23–22.91	6.98	0.031	09.80	19.62	10.98
(5)			10.25–39.12	19.71–22.91	7.98	0.024	08.98	19.42	10.90
(6)		$K_s$	20.21–34.84	20.67–22.28	1.29	0.048	15.78	20.14	11.35
(7)			10.48–34.84	18.98–22.28	5.98	0.052	05.26	17.48	10.27
(8)	Mrk 35	$J$	11.54–38.64	19.71–23.58	0.87	0.081	13.70	20.05	11.73
(9)			15.45–38.64	20.32–23.58	0.76	0.088	14.61	20.23	11.84
(10)			21.25–34.53	21.12–22.82	0.95	0.105	12.91	19.84	11.62
(11)		$K_s$	12.67–43.70	19.15–23.12	0.84	0.069	15.10	19.43	10.92
(12)			15.18–43.70	19.37–23.12	0.86	0.075	14.98	19.40	10.90
(13)			21.95–34.54	20.19–22.05	0.73	0.089	15.32	19.44	10.96

NOTE.—Columns 4, 5: radial interval and corresponding surface brightness interval for the Sérsic fit; col 6: best-fit shape parameter  $n$ ; col 7: rms scatter of the fit; cols 8, 9: best-fit effective radius and effective surface brightness; col 10: total magnitude of the LSBC derived from the fit.

increase in the rms.

In Fig 2 we show three apparently equally good fits: (1), (2) and (5) from Table 4.

- **Mrk 35** — Mrk 35 resembles closely Mrk 33 with respect to its LSBC morphology and the radial extent of its star-forming component ( $R \simeq 20''$ ). However, at variance to Mrk 33, decreasing the minimum fitting radius to  $R \simeq 12''$  has nearly no effect on the Sérsic exponent  $n$ . Fits done in different radial ranges and in the three NIR bands all give consistent results, with  $n \simeq 0.8-0.9$ . Thus, the LSBC of Mrk 35 appears to be well described by a Sérsic law very close to an exponential, and whose parameters do not depend significantly on the band or on the selected radial range.

#### *Sensitivity to sky subtraction errors*

Another important source of uncertainties on the Sérsic exponent  $n$  is associated with sky-subtraction errors, which can significantly change the SBP slope in its outermost parts. For an overestimate of the sky-background, the SBP will curve down, so that the derived  $n$  will be lower, and the total magnitude of the fitted Sérsic model fainter and for an underestimate of the sky-background, the profile will become flatter, so that the fitted  $n$  will be higher and the total magnitude brighter.

We checked the importance of this effect on Mrk 33 and Mrk 35. We first recomputed their  $J$  profiles by adding a constant offset  $\pm\Delta_{\text{sky}}$  to the input images. The term  $\Delta_{\text{sky}}$  was chosen so as to

change the intensity of the outermost datapoint of the SBP ( $\mu_J = 23.68 \text{ mag}/\square''$  at  $R = 49.90''$  for Mrk 33 and  $\mu_J = 23.58 \text{ mag}/\square''$  at  $R = 38.64''$  for Mrk 35) by 25% ( $\simeq 0.25 \text{ mag}$ ). The Sérsic parameters fitted to these SBPs are compared with those derived in the original SBP in Table 5.

We can see that, when the fit is not well constrained, as is the case for Mrk 33, even modest *systematic* uncertainties of  $\leq 0.25 \text{ mag}$  in the outer SBP portion can change  $n$  by a factor of 2, and model-dependent estimates of the total magnitude by 0.3 mag. For the case studied here, the  $r_e$  and  $\mu_e$  appear to be more stable.

Mrk 35, which shows a nearly exponential slope in its LSBC, appears to be more robust against sky-subtraction errors with respect to its  $n$ .

#### *4.2.2. Can the superposition of two different stellar populations mimic a Sérsic profile?*

As seen before, good Sérsic fits can be obtained even when the fitted radius interval includes a significant portion of the starburst component. So it is natural wondering whether the sum of two stellar populations differing in their  $M/L$  and radial distribution may reproduce a Sérsic profile with an exponent  $n$  significantly larger than that of its constituents. If true, this would imply that a satisfactory Sérsic fit does not rule out the existence of two or more distinct major stellar populations, and Sérsic model parameters may give a misleading description of the actual photometric structure of a galaxy.

This in turn means that one must be careful when using the exponent  $n$  from a fit to the whole light profile to make a com-



TABLE 5

SÉRSIC PARAMETERS FOR MRK 33 AND MRK 35 FOR AN IMPERFECTLY SUBTRACTED SKY BACKGROUND.

Profile	Radial range arcsec	Surface brightness range mag/□''	$n$	rms mag	$r_e$ arcsec	$\mu_e$ mag/□''	$m_{\text{LSBC}}$ mag
Mrk 33 - $J$ band							
original	20.47–49.90	21.23–23.68	2.09	0.041	17.76	20.99	11.68
sky under-subtracted	20.47–49.90	21.20–23.43	3.91	0.036	17.23	20.87	11.32
sky over-subtracted	20.47–49.90	21.26–24.01	1.33	0.048	18.15	21.08	11.95
Mrk 35 - $J$ band							
original	15.45–38.64	20.32–23.58	0.76	0.088	14.61	20.23	11.84
sky under-subtracted	15.45–38.64	20.31–23.33	0.88	0.081	14.51	20.19	11.74
sky over-subtracted	15.45–38.64	20.33–23.91	0.64	0.098	14.79	20.28	11.94

parative analysis of the structure of different classes of galaxies or of galaxies at different redshifts. For instance, assume for sake of discussion  $n = 3$ : this could be just a normal bulge, or a galaxy actually formed by starburst and a host component whose cumulative light distribution mimics well a Sérsic profile. The presence of two distinct components may go undetected because of poor resolution, faintness, or just because a very large sample is being analyzed in some automated way, and no visual inspection of each object is done. A similar effect has been observed by Balcells, Graham, Domínguez-Palmero, & Peletier (2003): "fits to ground-based profiles reach Sérsic indices  $n > 4$  because the light from HST-unresolved central sources, plus in some instances nuclear disks or bars, when convolved with typical ground-based seeing, link smoothly with the extended bulge profile and mimic higher  $n$  Sérsic profiles".

A real-life example is offered by the

BCD VII Zw 403. The ongoing star-forming activity in this system is indicated by H $\alpha$  emission, traceable in the inner  $\gtrsim 0.5$  kpc (Silich et al. 2002; Papaderos et al. 2002). Color magnitude diagram *HST* studies (Lynds et al. 1998; Schulte-Ladbeck et al. 1999) and ground-based optical photometry (Papaderos et al. 2002) show that the young blue stellar population is embedded into an old, more extended LSB component. Deep surface photometry down to  $\mu_B \simeq 28$  mag/□'' indicates that the LSB emission of VII Zw 403 can be well approximated by an exponential law (Papaderos et al. 2002).

Here we have reanalyzed the  $B$  band profile derived in this latter study, now using a Sérsic model to fit the LSBC of VII Zw 403. A model with  $n = 0.97$  yields an excellent fit in the radius range  $36'' < R < 80''$ ; by subtracting it from the observed profile, we can recover the intensity profile of the more centrally concentrated starburst population, which in

turn is well fitted by another Sérsic function with  $n = 0.86$ . The inner luminosity component is due to a young stellar population as indicated by its blue optical colors (Lynds et al. 1998; Papaderos et al. 2002). Hence, the observed SBP of VII Zw 403 is well described by the superposition of two nearly exponential profiles (bottom panel in Fig 3), each representing a very different stellar population with respect to age and  $M/L$ .

Notwithstanding this fact, if our light profile were truncated at  $\mu_B \lesssim 26.3$  mag/□″ ( $R \simeq 50''$ ), a single Sérsic model with  $n = 3.40$  would successfully fit the observed SBP in the range  $5'' < R < 50''$  (upper panel in Fig 3). So, if somebody were dealing with less deep profiles and lacking additional information on the galaxy, such as color maps or narrow-band images, they would perhaps conclude that this galaxy has just a single component with a Sérsic index  $n \sim 3.5$ .

This underlines once more the necessity for examining all available observational evidence (morphology, color profiles, ionized gas distribution, etc.) prior to profile fitting and decomposition, as well as the crucial importance of deep surface photometry studies for obtaining an unbiased description of the underlying host galaxy of BCDs.

### 4.3. Deriving the photometric parameters

Taking the above remarks into account, we proceeded to fit Sérsic models to the SBP of the galaxies in our sample. To minimize the risk that the choice of the fitted intervals were influenced by a subjective judgment or expectation on the results and

quality of the fit, one of the authors selected the radial interval upon inspection of the color and H $\alpha$  maps, and of the SBP (in order to exclude those outermost data-points with large error bars and obviously deviating from the profile’s general trend); another author ran the fitting algorithm within the prescribed radius intervals.

The results are listed in Table 6; a quick inspection does confirm that Sérsic fits to the SBP can in some cases give very different parameters in the three bands,  $n$  varying for a single object by up to one dex (Mrk 36). Solutions with Sérsic exponents  $n \gtrsim 15$  are omitted, because such fits fail to produce meaningful results, a general fact already noted by Graham et al. (1996).

These uncertainties in the derived Sérsic parameters propagate into large uncertainties in the model-dependent total magnitudes ( $m_{\text{LSBC}}$ ) of the LSBC. As a result, the integral color derived for the underlying host galaxy from subtraction of the  $m_{\text{LSBC}}$  in different bands can in many cases be incompatible with the observed ones (those derived directly from the CP, see next section), and cannot be accounted for by any stellar population (e.g. Mrk 33 with  $(J - H)_{\text{LSB}} = -0.23$  together with  $(J - K_s)_{\text{LSB}} = 0.20$ ).

Due to the failure of the Sérsic law to produce robust and self-consistent models for a large fraction of the available SBPs, it appears worthwhile to check whether a fixed  $n = 1$  (exponential model) allows for more a stable approximation to the LSBC.

We start off by repeating the test already done for the Sérsic law for Mrk 33, that is, we fit again its  $J$  and  $K_s$  SBP within the same radius intervals, this time after fixing  $n = 1$ . The results, listed in

TABLE 6  
SÉRSIC PHOTOMETRIC PARAMETERS FOR THE LSB HOST GALAXY

Galaxy	Band	Radial range arcsec	Surface brightness range mag/□''	$n$	$r_e$ arcsec	$\mu_e$ mag/□''	$m_{LSBC}$ mag
Mrk 33	$J$	16.89–42.57	20.84–23.23	2.88	15.34	20.64	11.49
	$H$	16.26–22.83	20.38–21.33	0.90	13.44	20.01	11.72
	$K_s$	16.09–29.89	20.13–21.77	1.38	15.06	20.03	11.29
Mrk 35	$J$	21.25–34.53	21.12–22.82	0.97	12.72	19.80	11.59
	$H$	21.30–42.88	20.49–23.30	0.80	15.88	19.91	11.31
	$K_s$	21.95–43.70	20.19–23.12	1.01	13.33	19.03	10.70
Mrk 36	$J$	07.44–11.30	21.46–22.77	9.46	0.37	13.95	12.25
	$H$	07.55–12.37	21.17–22.50	0.74	7.34	21.14	14.26
	$K_s$	07.86–11.34	20.98–22.03	1.73	4.67	19.78	13.46
UM 462	$J$	08.63–21.40	20.86–23.12	1.20	8.63	20.82	13.35
	$H$	08.04–21.52	20.23–22.59	1.50	9.02	20.39	12.72
	$K_s$	08.16–11.73	19.98–20.65	0.57	8.90	20.12	12.94
II Zw 70	$J$	10.04–25.77	21.57–24.76	2.30	5.09	19.98	13.34
	$H$	10.17–22.31	21.19–23.83	2.19	5.38	19.72	12.98
	$K_s$	09.88–22.52	20.88–23.82	1.35	6.57	20.07	13.14
II Zw 71	$J$	18.55–27.51	21.71–22.94	0.70	14.77	21.27	12.89
	$H$	18.74–27.26	21.34–22.71	0.34	15.36	21.02	12.89
	$K_s$	16.11–27.07	20.82–22.36	0.46	15.41	20.79	12.52
I Zw 123	$J$	08.34–11.06	21.57–22.46	> 15	...	...	...
	$H$	07.68–09.58	20.73–21.45	> 15	...	...	...
	$K_s$	06.30–09.17	19.95–21.45	0.29	5.11	19.67	14.01
Mrk 297	$J$	20.42–34.31	21.45–24.10	> 15	...	...	...
	$H$	20.36–29.29	21.29–23.30	2.94	1.37	12.21	08.31
	$K_s$	18.70–26.84	20.41–22.52	> 15	...	...	...

Table 7, show that exponential fits give parameters consistent in the different bands, and are not that sensitive to the selected radial range (provided it does not include the starburst), nor to sky-subtraction errors, as compared with Sérsic models.

The fitted parameters to the LSBC of all sample galaxies using an exponential model are listed in Table 8. At variance to what we found for the Sérsic models, the integral colors of the LSBC, as obtained from exponential fits, are consistent within the errors with the colors derived directly from color profiles.

We note that this improvement in the stability of the fit results is due to having set  $n$  equal to a constant (thus removing one degree of freedom in the Sérsic law), not to some particular property of the exponential model. Indeed, fixing any other value within reasonable intervals, would give comparable improvements in the fit stability.

#### 4.4. Colors of the underlying stellar host galaxies and age estimation

Upon inspection of the CPs in Figure 1 we see that the galaxies present constant colors in their outer regions, in agreement with the results found in the optical (Papers I and II). The good quality of our data allowed us to derive reliable colors for the LSBC of the BCDs. They have been computed by averaging the color profiles over a radial range which excludes the starburst-dominated regions (i.e., for  $R \geq R_{\text{transition}}$ ) and those outermost data-points having large error bars. The resulting values, corrected from Galactic extinction as described in Section 3.1, are dis-

played in Table 9.

To obtain an estimate of the ages of LSBCs, we compared their colors with the predictions of the GALEV spectrophotometric evolutionary synthesis models (Schulz et al. 2002, Anders, Bicker & Fritze-v.Alvensleben, priv. comm.). An initial mass function with a Salpeter slope and lower and upper cutoff masses of 0.08 and 100  $M_{\odot}$  was chosen.

Figure 4 displays the  $(V-J)-(J-H)$  diagram for the LSBC of the sample galaxies, together with the tracks of the models for an instantaneous burst (IB) with metallicities  $Z = 0.02 Z_{\odot}$  and  $Z = 0.4 Z_{\odot}$ , as well as for a continuous star-formation (CSF) rate with the same metallicities. Most of the galaxies seem to present colors compatible with the models predictions. In the IB approximation, the ages of the LSBC are estimated to be  $\gtrsim 3$  Gyr, whereas, as expected, ages are larger in the CSF approximation.

Two of the objects, Mrk 33 and Mrk 297, which happen to be the most luminous galaxies in the sample, lie far off the model tracks. A detailed study of the evolutionary status and stellar composition of these BCDs is outside the scope of the present paper. In fact a proper characterization of their stellar population, done by combining multiband images and spectra, will be the subject of the next paper in this series.

## 5. Comments on the Individual Galaxies

*Mrk 33.* — Mrk 33 is a luminous BCD with a regular appearance, belonging to the *Type I* (nuclear starburst) BCD class introduced in Paper II; the star-

TABLE 7  
MRK 33: PARAMETERS FOR THE EXPONENTIAL MODEL

Fit ID	Band	Radial range arcsec	Surface brightness range mag/□''	rms mag	$\alpha$ arcsec	$\mu_0$ mag/□''	$m_{\text{LSBC}}$ mag
(1)	<i>J</i>	20.47–49.90	21.23–23.68	0.061	13.44	19.72	12.07
(2)		10.25–49.90	19.71–23.68	0.180	11.16	19.12	11.87
(3)		21.29–39.12	21.40–22.91	0.040	12.88	19.63	12.08
(4)		20.47–39.12	21.23–22.91	0.047	12.63	19.58	12.07
(5)		10.25–39.12	19.71–22.91	0.144	09.98	18.89	11.89
(6)	<i>J</i> , sky under-subtracted	20.47–49.90	21.20–23.43	0.069	14.75	19.86	12.01
(7)	<i>J</i> , sky over-subtracted	20.47–49.90	21.26–24.01	0.053	12.06	19.53	12.12
(8)	<i>K<sub>s</sub></i>	20.21–34.84	20.67–22.28	0.049	10.06	18.50	11.48
(9)		10.48–34.84	18.98–22.28	0.124	08.65	18.02	11.32

NOTE.—For the exponential law there is a direct relation between the effective parameters  $r_e$  and  $\mu_e$  and the scale factors  $\alpha$  and  $\mu_0$ :  $\alpha = 0.596 R_e$  and  $\mu_0 = \mu_e - 1.822$

burst activity is confined to the inner regions of a smooth, red stellar LSBC. It is a well studied galaxy, with a metallicity of about  $1/3 Z_{\odot}$  (Davidge 1989; Legrand et al. 1997). Kunth & Joubert (1985) reported the presence of a large number of Wolf-Rayet (WR) stars in its center, while Lequeux et al. (1995) and Legrand et al. (1997) reported evidence for a strong outflow of gas, ejected from the starburst region at velocities close to  $200 \text{ km sec}^{-1}$ . To study its stellar population, Fanelli, O’Connell, & Thuan (1988) analyzed the UV spectrum and concluded that the present burst of SF has been preceded by at least two other episodes, the most recent of which ended not more than 20 Myr ago. Krüger, Fritze-v. Alvensleben, & Loose (1995) obtained also a good fit to the optical and NIR continuum by assuming that a 5 Myr long starburst took place in a galaxy which had been forming

stars continuously, but at a lower rate, during the last 15 Gyr. Mas-Hesse & Kunth (1999) estimated an age of 4.5 Myr for the present starburst.

The morphologies in the NIR and in the optical basically coincide, though in the optical the inner isophotes, clearly affected by the presence of dust, have a much more irregular appearance than in the NIR. Also, in the NIR we can better distinguish two peaks in the central starburst, aligned in the southeast-northwest direction; their positions coincide with the knots visible in the optical color maps (see Paper II).

The  $V-K$  color morphology of Mrk 33 (Figure 5) is markedly different from that seen on optical color maps (see Paper II). An inhomogeneous extinction pattern in the inner portions of the galaxy, already noticed in the optical (Moellenhoff, Hum-

TABLE 8  
STRUCTURAL PARAMETERS OF THE LSB HOST GALAXY FROM EXPONENTIAL FITS.

Galaxy	Band	Radial range arcsec	Surface brightness range mag/□''	$\alpha$ arcsec	$\mu_0$ mag/□''	$m_{\text{LSBC}}$ mag
Mrk 33	<i>J</i>	16.89–42.57	20.84–23.23	12.03	19.43	12.02
	<i>H</i>	16.26–22.83	20.38–21.33	7.86	18.14	11.66
	<i>K<sub>s</sub></i>	16.09–29.89	20.13–21.77	9.54	18.35	11.45
Mrk 35	<i>J</i>	21.25–34.53	21.12–22.82	7.45	17.93	11.56
	<i>H</i>	21.30–42.88	20.49–23.30	8.34	17.71	11.10
	<i>K<sub>s</sub></i>	21.95–43.70	20.19–23.12	8.05	17.26	10.72
Mrk 36	<i>J</i>	07.44–11.30	21.46–22.77	3.34	19.09	14.47
	<i>H</i>	07.55–12.37	21.17–22.50	4.21	19.23	14.10
	<i>K<sub>s</sub></i>	07.86–11.34	20.98–22.03	3.47	18.53	13.82
UM 462	<i>J</i>	08.63–21.40	20.86–23.12	5.43	19.13	13.45
	<i>H</i>	08.04–21.52	20.23–22.59	5.88	18.76	12.91
	<i>K<sub>s</sub></i>	08.16–11.73	19.98–20.65	5.73	18.44	12.64
II Zw 70	<i>J</i>	10.04–25.77	21.57–24.76	5.35	19.66	14.02
	<i>H</i>	10.17–22.31	21.19–23.83	5.15	19.14	13.58
	<i>K<sub>s</sub></i>	09.88–22.52	20.88–23.82	4.67	18.74	13.38
II Zw 71	<i>J</i>	18.55–27.51	21.71–22.94	7.94	19.17	12.67
	<i>H</i>	18.74–27.26	21.34–22.71	6.76	18.26	12.11
	<i>K<sub>s</sub></i>	16.11–27.07	20.82–22.36	8.13	18.66	12.10
I Zw 123	<i>J</i>	08.34–11.06	21.57–22.46	3.40	18.95	14.29
	<i>H</i>	07.68–09.58	20.73–21.46	2.52	17.51	13.49
	<i>K<sub>s</sub></i>	06.30–09.17	19.96–21.45	2.07	16.58	12.99
Mrk 297	<i>J</i>	20.42–34.31	21.45–24.10	5.87	17.90	12.05
	<i>H</i>	20.36–29.29	21.29–23.30	4.86	16.80	11.36
	<i>K<sub>s</sub></i>	18.70–26.84	20.41–22.52	4.20	15.67	10.54

TABLE 9  
 COLORS OF THE LSB HOST GALAXY

Galaxy	$V-J$	$V-H$	$V-K$	$J-H$	$H-K$	$J-K$
Mrk 33	$2.01 \pm 0.04$	$2.25 \pm 0.09$	$2.52 \pm 0.05$	$0.34 \pm 0.07$	$0.27 \pm 0.08$	$0.51 \pm 0.05$
Mrk 35	$1.55 \pm 0.06$	$2.17 \pm 0.05$	$2.44 \pm 0.05$	$0.57 \pm 0.08$	$0.30 \pm 0.05$	$0.87 \pm 0.06$
Mrk 36	$1.35 \pm 0.12$	$1.90 \pm 0.11$	$2.00 \pm 0.07$	$0.45 \pm 0.12$	$0.19 \pm 0.10$	$0.64 \pm 0.08$
UM 462	$1.41 \pm 0.09$	$1.97 \pm 0.19$	...	$0.57 \pm 0.13$	$0.19 \pm 0.13$	$0.77 \pm 0.03$
II Zw 70	$1.49 \pm 0.07$	$1.90 \pm 0.08$	$2.02 \pm 0.13$	$0.40 \pm 0.04$	...	$0.55 \pm 0.08$
II Zw 71	$1.57 \pm 0.09$	$1.91 \pm 0.09$	$2.16 \pm 0.08$	$0.38 \pm 0.03$	$0.18 \pm 0.02$	$0.57 \pm 0.04$
I Zw 123	$1.43 \pm 0.03$	...	...	$0.46 \pm 0.12$	...	$0.78 \pm 0.09$
Mrk 297	$1.57 \pm 0.19$	$1.81 \pm 0.10$	$2.03 \pm 0.08$	$0.18 \pm 0.08$	$0.31 \pm 0.05$	$0.51 \pm 0.06$

NOTE.—Columns 2-7: mean optical-NIR and NIR colors, corrected for Galactic extinction, of the LSB of the sample galaxies, as derived from their color profiles.

mel & Bender 1992; Paper II), is confirmed by our color maps: a conspicuous red patch is seen at the south-east of the galaxy center. Interestingly, the bluest regions do not coincide with the brightest (central) knot, as it was found to be the case in optical color maps, but appear displaced to the south.

We have performed aperture photometry centered on the red peak, within a circular aperture of radius  $2''$ , and determined its colors:  $V-J = 2.18$ ,  $V-H = 2.74$ ,  $V-K = 3.00$ ,  $J-H = 0.56$ ,  $H-K = 0.26$ . Such optical-NIR colors, which are even redder than those in the LSB component (see Table 9), can naturally be explained by dust extinction. This is also supported by recent interferometric  $^{12}\text{CO}$  studies of Mrk 33 revealing a morphologically and kinematically complex molecular gas distribution in its inner part, also pointing to a high, non-uniform absorption (Fritz 2000).

*Mrk 35.* — This is another luminous, high-metallicity BCD, with an oxygen abundance  $Z_{\odot}/3$  (Steel et al. 1996), which belongs to the *Type III* (chain starburst) morphological class introduced in Paper II. The star-forming activity is distributed along the northeast-southwest direction, in a bar-like structure. The brighter star-forming regions are placed in the central part of the galaxy, and form a "heart-shaped" structure; a tail departs from it to the south-west, connecting with two moderately bright knots  $\sim 20''$  further away. We have labeled the knots resolved in the broad-band frames following Mazzarella & Boroson (1993) (see Figure 1). Steel et al. (1996) reported the presence of Wolf-Rayet stars in the knot **a**, and inferred for it an age younger than 5 Myr.

The morphology in the optical and NIR broad-band frames is similar. Optical frames present more distorted inner isophotes, which point to the presence of

dust. Interestingly, the central knot, **b**, coincides with the intensity peak in the NIR, whereas knot **a** is identifiable with the optical maximum. The intensity ratio between knots **a** and **b** decreases when moving from the  $U$  to the  $K_s$  band. A similar behavior has been reported so far only in the BCD Mrk 178 by Noeske et al. (2003).

Figure 6 displays the  $V-K$  color map of Mrk 35, which reveals a very intriguing morphology: a dust lane is crossing the center of the galaxy in the north-south direction, bending eastwards to the south. The **a** knot has blue colors, while the inner knots **b** and **c** are very red.

*Mrk 36.* — It is a typical compact, low-luminosity and low-metallicity BCD, classified as *Type I* (nuclear starburst). Star-forming activity takes place in the inner regions of a roughly elliptical LSBC with redder colors. It has been shown (Paper II), from high-resolution ground-based optical imagery, that star formation occurs in at least five compact (diameter  $\lesssim 200$  pc) Super-Star Cluster (SSC) candidates spread over the inner region of the galaxy. This finding is confirmed by our infrared data. The ages of these star-forming knots, derived from optical colors, range between 2.5 and 5 Myr (Mas-Hesse & Kunth 1999; Cairós 2000).

*UM 462.* — This is another low-luminosity, low-metallicity system, with  $12 + \log(O/H) = 7.95 \pm 0.01$  (Izotov & Thuan 1999). It falls into the *Type II* (extended starburst) morphological class. It exhibits an intriguing morphology in its star-forming region, which is resolved into six knots. These features were not detected in our previous optical data (Paper I) due to poor seeing conditions.

Vanzi, Hunt, & Thuan (2002) have recently published NIR spectra and images of this galaxy. In Figure 1 we labeled the star-forming knots following the notation used by the above authors, who identified them with SSCs. Photometry within apertures of  $2''$  in radius is listed in Table 10. These values have been corrected only for Galactic extinction; no corrections have been made for the ionized gas contribution nor for the contribution of the underlying LSBC. Our results are in fair agreement with the values published by Vanzi, Hunt, & Thuan (2002).

*II Zw 70.* — This is a *Type I* (nuclear starburst) galaxy, which forms together with II Zw 71 a pair of interacting galaxies (Vorontsov-Vel'Yaminov 1977). Evidence for an ongoing interaction between both systems is presented by interferometric H I studies (Balkowski, Chamaraux, & Weliachew 1978; Cox et al. 2001). A conspicuous central star-forming region is placed in the center of a markedly elongated LSBC, with a nearly constant ellipticity of  $\approx 0.7$ . An extended, extraordinarily faint ( $\mu_B \gtrsim 27$  mag/ $\square''$ ) stellar plume emerging from the star-forming region and protruding  $\sim 1.7$  to the direction of II Zw 71 has been recently discovered on deep optical images (Papaderos et al. 2001; Cairós et al. 2003). It apparently coincides with the massive H I stream connecting II Zw 70 with II Zw 71; its relatively blue optical colors are consistent with the hypothesis that it has recently formed within the gaseous bridge between the BCDs. The  $V-K$  color map of II Zw 70 is shown in Figure 7.

*II Zw 71.* — This galaxy belongs to the *Type III* (chain starburst) morphological



TABLE 10  
 COLORS OF STAR-FORMING KNOTS IN UM 462

Knot	$J-H$ (mag)	$H-K$ (mag)
1	0.34	0.43
2	0.44	0.29
3	0.39	0.35
4	0.43	0.29
5	0.48	0.25
6	0.43	0.29

class. The interpretation of II Zw 71 as a (possible) polar ring galaxy (Whitmore et al. 1990) has recently received further observational support through the analysis by Cox et al. (2001). Its LSBC presents red colors and elliptical isophotes, however the chain of star-forming regions, aligned perpendicular to the major axis of the LSBC, results in an overall distorted morphology. The  $B-K$  color map of this system is shown in Figure 8.

*I Zw 123.* — It is a small and compact *Type I* class BCD, with a metallicity of  $Z_{\odot}/7$  (Izotov, Thuan, & Lipovetsky 1997). It presents a regular morphology, with its star formation occurring atop the central part of a roughly circular LSB envelope, whose ellipticity is about 0.1. This central star-forming region is resolved into two smaller knots. Knot **a** is slightly displaced from the center of the outer isophotes and shows a slight north-west elongation; **a** seems to be connected by a "bridge-structure" with the southern knot **b**. Feather-like extensions can be seen to the northeast and southwest; they show very red colors, and are not detected in

$H\alpha$  frames (Noeske et al. 2001), so they are most likely background objects.

*Mrk 297.* — This object (*Type II*: extended starburst), originally discussed in the Thuan & Martin (1981) list and included in several subsequent studies of BCDs, strictly speaking should not be regarded as a dwarf galaxy ( $M_B = -20.54$ , Paper II). Alloin & Dufloc (1979) classified it as a merging system. Indeed, the galaxy is very distorted and shows in its LSBC filamentary north-south extensions, suggestive of an ongoing merger event.

*Mrk 297* presents a very intriguing morphology. Its intensity distribution peaks in the center of the galaxy. Smaller knots form a chain aligned in the east-west direction. The  $H\alpha$  maps (see Paper II) show that the SF is taking place in numerous regions spread over nearly the entire galaxy. Ground-based  $V-K$  (see Figure 9) and HST  $V-R$  color maps (Papaderos 1998) clearly indicate a large-scale, inhomogeneous absorption pattern in the galaxy.

*Mrk 407.* — It is a very compact and faint *Type I* BCD. It presents an overall regular morphology, though its outer

isophotes are slightly perturbed and elongated along the northwest–southeast direction. The quality of the NIR images does not permit to tell whether or not an older stellar LSBC is underlying its star-forming regions.

## 6. Discussion

From the results of the fits listed in Table 6, it is evident that the Sérsic law, while allowing for a more precise description of the intensity distribution of many LSBCs, still has serious drawbacks, such as the sensitivity of the model parameters to the fitted radial range. Furthermore, in several cases the derived Sérsic indices for the same galaxy may be quite different in various passbands. Given that color gradients within the LSBC of evolved BCDs are small, we would expect to obtain similar Sérsic solutions regardless of the passband.

Only in two of the nine sample BCDs, namely Mrk 35 and II Zw 70, the fit is reasonably good and stable. For UM 462 the fits in  $J$  and  $H$  are in agreement; the discrepant parameters obtained for  $K_s$  are probably due to the poorer quality of the data.

What does all this mean? Should we principally discard the Sérsic law as a physically meaningful representation of the SBPs of the host galaxy of BCDs, and hence look for alternative fitting formulas? Or, more simply, are observational uncertainties/limitations of the data responsible for the failure of the Sérsic law to provide an effective description of the photometric structure of the LSBC? At this stage an answer to the above questions is premature. A more comprehensive analysis must

be carried out on accurate SBPs derived from deep multiwavelength data; this will be done in a forthcoming paper.

The first and immediate conclusion we can draw from this analysis is that one should exercise extreme caution when fitting the Sérsic law in BCDs and, even more importantly, when fitted parameters are discussed in the context of the physical state of the stellar LSBC component or the dark matter distribution of a BCD. We suspect that the problems so far discussed are the reason for the surprisingly high Sérsic exponents derived by Bergvall & Östlin (2002) for the LSBC of BCDs: in four of the six galaxies they studied they infer a  $n > 17$  (see their Table 5). It is hardly imaginable that such values, exceeding even those found among the brightest elliptical galaxies (Graham et al. 1996), are witnessing a particular type of dynamical equilibrium of the visible and dark matter in BCDs (see discussion in Bergvall & Östlin 2002).

We would like to highlight some results that have emerged from the present study. First, in some galaxies the profile of the LSBC presents a clear curvature in the  $R - \mu$  diagram (Mrk 33 and II Zw 70), and the exponential law gives a poor fit to their SBP; in other BCDs (Mrk 35 and UM 462), however, the LSBC seems to be well fit by the exponential law. This variation in the profile shape might indicate that the structure of the LSBC is not the same in all BCDs, a result already suggested by the findings of previous work (Loose & Thuan 1986; Kunth, Maurogordato, & Vigroux 1988; Kunth & Östlin 2000; Noeske et al. 2000; Cairós 2000; Cairós et al. 2002; Bergvall & Östlin 2002).

Therefore, the "so called" BCD are objects with an active starburst which dominates their optical properties, but when the characteristic of LSBC are taken into account, they seem to constitute an heterogeneous class of galaxies.

Second, it is clear that an incorrect modeling of the underlying stellar component would yield a misleading physical description not only for the LSB component itself, but also for the superposed starburst component. We see comparing the results from Tables 6 and 8 that fitting different models to the LSBC one obtains total LSBC luminosities differing by several tenths of a magnitude (see for instance Mrk 33 in  $J$ ). Therefore, as pointed out in Cairós et al. (2002) and Papaderos et al. (2002), a proper modeling of the radial intensity distribution of the LSBC is essential for an accurate derivation of the star formation history within the starburst component.

In the 8 galaxies in which a LSBC has been identified, the colors of the latter suggest old ages. However, two of the galaxies, Mrk 33 and Mrk 297, show colors which place them in a different part of the two-color diagram (Fig. 4), far from the region populated by other BCDs and described by simple star formation histories. These two galaxies are the two most luminous in the sample; according to a strict classification criterion, they should not be considered dwarf, but belong to the class of Luminous Blue Compact Galaxies (LBCG) (Östlin 1998, Paper II).

Finally, the fact that we found inhomogeneous, large-scale dust absorption in three of the nine galaxies challenges the belief that dust is generally of no concern in

BCD studies. This should be taken into account, especially when interpreting ages of BCDs using color-magnitude diagrams.

## 7. Summary and Conclusions

This is the third of a series of papers devoted to a multiwavelength study of a large sample of BCD galaxies. In the first two papers we presented optical broad- and narrow-band observations of the galaxy sample. Here we have extended our dataset with broad-band  $J$ ,  $H$  and  $K_s$  NIR images for 9 BCDs. We have derived contour maps in the  $J$  band, as well as surface brightness and color profiles. We have also shown optical-NIR color maps for several objects.

The main results of our work can be summarized as follows:

- The galaxies present very similar morphologies in the NIR and in the optical. The presence of two distinct components, already seen in previous optical studies, is also discernible in the NIR surface brightness profiles in all but one case (Mrk 407): a young starburst population, dominating the inner regions, is superposed on the host galaxy, detectable at faint surface brightness levels (typically  $\mu \gtrsim 21$  mag/arcsec<sup>2</sup> in  $J$ ). The host galaxy exhibits in its outer regions quite regular elliptical isophotes and nearly constant red colors, indicative of an evolved stellar population. In Mrk 407, the present data do not allow to verify the presence of an old underlying low-surface brightness component (LSBC).
- We have checked whether a Sérsic

fit to the outer part of SBPs can be used to parametrize the structural properties of the underlying LSBC. At least two of the sample BCDs (namely, Mrk 33 and II Zw 70), show a clear curvature in their profiles in the  $R - \mu$  diagram, suggesting a best-fitting Sérsic exponent  $n > 1$ , whereas in two other galaxies (Mrk 35 and UM 462) the LSBC profiles are consistent with an exponential law ( $n = 1$ ). We have discussed at length the problems emerging from profile fitting using the Sérsic law, and shown that the usable surface brightness interval of the available SBPs does generally not allow to tightly constrain the Sérsic parameters. The latter were found to be very sensitive to the fitted radial range and to uncertainties in the sky subtraction.

In addition we found that a good Sérsic profile is not an unambiguous proof of a monocomponent stellar system; we demonstrate that such a profile can be produced by the superposition of a young stellar component on an old, more extended LSBC with an exponential profile. We emphasize that one must not underestimate the various sources of uncertainties affecting Sérsic fits to composite and in many respects very complex extragalactic systems, such as BCDs. We therefore recommend against just using the apparently excellent quality of Sérsic fits to a wide range of observed surface brightness distributions to derive astrophysical results or inferences.

We have argued that an exponential model, while it may not be a universal descriptor of the intensity distribution of the LSBC, it nonetheless appears to be considerably more stable against the above mentioned problems. Therefore it can provide, at this stage, a more reliable tool to quantify the structural parameters of the LSBC and compare them with those of other nearby dwarf classes, as well as with star-forming galaxies at a larger redshift.

- Optical-NIR color maps indicate a large-scale inhomogeneous absorption in three of the sample galaxies.

Based on observations with the WHT operated on the island of La Palma by the Royal Greenwich Observatory in the Spanish Observatorio del Roque de los Muchachos of the Instituto de Astrofísica de Canarias and on observations taken at the German-Spanish Astronomical Center, Calar Alto, Spain, operated by the Max-Planck-Institut für Astronomie (MPIA), Heidelberg, jointly with the spanish "Comisión Nacional de Astronomía". We thank the staff of both observatories. We thank Dr. A.W. Graham for his valuable comments and discussions. We thank J. N. González-Pérez for his help in the initial stages of this project. We thank Dr. Uta Fritze-v.Alvensleben, P. Anders, J. Bicker and J.Schulz for kindly providing the GALEV models. This work has been partially funded by the spanish "Ministerio de Ciencia y Tecnología" (grants AYA2001-3939 and PB97-0158). L. M. Cairós acknowledges support by the EC

grant HPMF-CT-2000-00774. Research by K.G.N. has been supported by the Deutsche Forschungsgemeinschaft (DFG) grant FR325/50-1. N. Caon thanks the Universitäts-Sternwarte of Göttingen for its kind hospitality. This research has made use of the NASA/IPAC Extragalactic Database (NED), which is operated by the Jet Propulsion Laboratory, Caltech, under contract with the National Aeronautics and Space Administration.

## REFERENCES

- Alloin, D. & Duflot, R. 1979, *A&A*, 78, L5
- Alton, P. B., Draper, P. W., Gledhill, T. M., Stockdale, D. P., Scarrott, S. M., & Wolstencroft, R. D. 1994, *MNRAS*, 270, 238
- Andredakis, Y. C., Peletier, R. F., & Balcells, M. 1995, *MNRAS*, 275, 874
- Balcells, M., Graham, A. W., Domínguez-Palmero, L., & Peletier, R. F. 2003, *ApJ*, 582, L79
- Balkowski, C., Chamaraux, P., & Welchew, L. 1978, *A&A*, 69, 263
- Beck, S. C., Kelly, D. M., & Lacy, J. H. 1997, *AJ*, 114, 585
- Bergvall, N. & Östlin, G. 2002, *A&A*, 390, 891
- Brosch, N., Heller, A., & Almozino, E. 1998, *MNRAS*, 300, 1091
- Cairós, L. M. 2000, PhD: Formation and Evolution of Blue Compact Dwarf Galaxies (Instituto de Astrofísica de Canarias, Spain)
- Cairós, L. M., Vílchez, J. M., González-Pérez, J. N., Iglesias-Páramo, J., & Caon, N. 2001a, *ApJS*, 133, 321 (= Paper I)
- Cairós, L. M., Caon, N., Vílchez, J. M., González-Pérez, J. N., & Muñoz-Tuñón, C. 2001b, *ApJS*, 136, 2 (= Paper II)
- Cairós, L. M., Caon, N., García-Lorenzo, B., Vílchez, J. M., & Muñoz-Tuñón, C. 2002, *ApJ*, 577, 164
- Cairós, L. M. et al. 2003 in preparation
- Caon, N., Capaccioli, M., & D’Onofrio, M. 1993, *MNRAS*, 265, 1013
- Cardelli, J. A., Clayton, G. C., & Mathis, J. S. 1989, *ApJ*, 345, 245
- Cox, A. L., Sparke, L. S., Watson, A. M., & van Moorsel, G. 2001, *AJ*, 121, 692
- Davidge, T. J. 1989, *PASP*, 101, 494
- Davies, J. I. & Phillipps, S. 1988, *MNRAS*, 233, 553
- Doublier, V., Comte, G., Petrosian, A., Surace, C., & Turatto, M. 1997, *A&AS*, 124, 405
- Doublier, V., Caulet, A., & Comte, G. 1999, *A&AS*, 138, 213
- Doublier, V., Caulet, A., & Comte, G. 2001, *A&A*, 367, 33
- Fanelli, M. N., O’Connell, R. W., & Thuan, T. X. 1988, *ApJ*, 334, 665
- Fritz, T. 2000, PhD Thesis, Rheinische Friedrich-Wilhelm Universität, Bonn

- Gil de Paz, A., Zamorano, J., Gallego, J., & Domínguez, F. d. 2000, *A&AS*, 145, 377
- González-Pérez, J. , Kidger, M. R., & Martin-Luis, F. 2001, *AJ*, 122, 2055
- Graham, A. W., Lauer, T. R., Colless, M., & Postman, M. 1996, *ApJ*, 465, 534
- Graham, A. W., Erwin, P., Caon, N., & Trujillo, I. 2001, *ApJ*, 563, L11
- Guzmán, R., Koo, D. C., Faber, S. M., Illingworth, G. D., Takamiya, M., Kron, R. G., & Bershady, M. A. 1996, *ApJ*, 460, L5
- Guzmán, R., Gallego, J., Koo, D. C., Phillips, A. C., Lowenthal, J. D., Faber, S. M., Illingworth, G. D., & Vogt, N. P. 1997, *ApJ*, 489, 559
- Izotov, Y. I., Thuan, T. X., & Lipovetsky, V. A. 1997, *ApJS*, 108, 1
- Izotov, Y. I. & Thuan, T. X. 1999, *ApJ*, 511, 639
- James, P. A. 1994, *MNRAS*, 269, 176
- Koo, D. C., Bershady, M. A., Wirth, G. D., Stanford, S. A., & Majewski, S. R. 1994, *ApJ*, 427, L9
- Koo, D. C., Guzman, R., Faber, S. M., Illingworth, G. D., Bershady, M. A., Kron, R. G., & Takamiya, M. 1995, *ApJ*, 440, L49
- Krüger, H., Fritze-v. Alvensleben, U., & Loose, H.-H. 1995, *A&A*, 303, 41
- Kunth, D. & Joubert, M. 1985, *A&A*, 142, 411
- Kunth, D. & Sargent, W. L. W. 1986, *ApJ*, 300, 496.
- Kunth, D., Maurogordato, S., & Vigroux, L. 1988, *A&A*, 204, 10.
- Kunth, D. & Östlin, G. 2000, *A&A Rev.*, 10, 1
- Legrand, F., Kunth, D., Mas-Hesse, J. M., & Lequeux, J. 1997, *A&A*, 326, 929
- Lequeux, J. & Viallefond, F. 1980, *A&A*, 91, 269.
- Lequeux, J., Kunth, D., Mas-Hesse, J. M., & Sargent, W. L. W. 1995, *A&A*, 301, 18
- Loose, H. H. & Thuan, T. X. 1986, in *Star Forming Dwarf Galaxies and Related Objects*, eds. D. Kunth, T. X. Thuan, J. T. T. Van (Gif-sur-Yvette: Editions Frontieres), 73
- Lynds, R., Tolstoy, E., O’Neil, E. J., & Hunter, D. A. 1998, *AJ*, 116, 146
- Makino, J., Akiyama, K., & Sugimoto, D. 1990, *PASJ*, 42, 205
- Marlowe, A. T., Meurer, G. R., Heckman, T. M., & Schommer, R. 1997, *ApJS*, 112, 285
- Marlowe, A. T., Meurer, G. R., & Heckman, T. M. 1999, *ApJ*, 522, 183
- Mas-Hesse, J. M. & Kunth, D. 1999, *A&A*, 349, 765
- Masegosa, J., Moles, M., & Campos-Aguilar, A. 1994, *ApJ*, 420, 576
- Mazzarella, J. M. & Boroson, T. A. 1993, *ApJS*, 85, 27

- Moellenhoff, C., Hummel, E. & Bender, R. 1992, *A&A*, 255, 35
- Noeske, K. G., Guseva, N. G., Fricke, K. J., Izotov, Y. I., Papaderos, P., & Thuan, T. X. 2000, *A&A*, 361, 33
- Noeske, K. G., Cairós, L. M., Papaderos, P., Vílchez, J. M., & Fricke, K. J. 2001, *Ap&SS*, 276, 901
- Noeske, K. G., Papaderos, P., Cairós, L. M., & Fricke, K. J. 2002, *A&A*, submitted
- Oconnell, R. W., Thuan, T. X., & Goldstein, S. J. 1978, *ApJ*, 226, L11
- Östlin, G. 1998, Ph.D. Thesis, Uppsala University, Sweden
- Östlin, G., Bergvall, N., & Rönneback, J. 1998, *A&A*, 335, 85
- Pagel, B. E. J., Simonson, E. A., Terlevich, R. J., & Edmunds, M. G. 1992, *MNRAS*, 255, 325
- Papaderos, P., Loose, H.-H., Thuan, T. X., & Fricke, K. J. 1996a, *A&AS*, 120, 207
- Papaderos, P., Loose, H.-H., Fricke, K. J., & Thuan, T. X. 1996b, *A&A*, 314, 59
- Papaderos, P. 1998, PhD Thesis, Universitäts-Sternwarte Göttingen, Germany
- Papaderos, P., Noeske, K. G., Cairós, L. M., Vílchez, J. M., & Fricke, K. J. 2001, Dwarf galaxies and their environment, 283
- Papaderos, P., Izotov, Y. I., Thuan, T. X., Noeske, K. G., Fricke, K. J., Guseva, N. G., & Green, R. F. 2002, *A&A*, 393, 461
- Peletier, R. F., Balcells, M., Davies, R. L., Andredakis, Y., Vazdekis, A., Burkert, A., & Prada, F. 1999, *MNRAS*, 310, 703
- Peletier, R. F., Valentijn, E. A., & Jameson, R. F. 1990, *A&A*, 233, 62
- Persson, S. E., Murphy, D. C., Krzeminski, W., Roth, M., & Rieke, M. J. 1998, *AJ*, 116, 2475
- Sargent, W. L. W. & Searle, L. 1970, *ApJ*, 162, L155
- Schlegel, D. J., Finkbeiner, D. P., & Davis, M. 1998, *ApJ*, 500, 525
- Schulte-Ladbeck, R. E., Hopp, U., Greggio, L., & Crone, M. M. 1999, *AJ*, 118, 2705
- Schulz, J., Fritze-v. Alvensleben, U., Möller, C.S. & Fricke, K. J. 2002, in press
- Silich, S., Tenorio-Tagle, G., Muñoz-Tuñón, C., & Cairós, L. M. 2002, *AJ*, 123, 2438
- Steel, S. J., Smith, N., Metcalfe, L., Rabbette, M., & McBreen, B. 1996, *A&A*, 311, 721
- Telles, J. E. 1995, Ph.D. Thesis, Univ. Cambridge, United Kingdom
- Telles, E. & Terlevich, R. 1997, *MNRAS*, 286, 183
- Thuan, T. X. & Martin, G. E. 1981, *ApJ*, 247, 823
- Thuan, T. X. 1985, *ApJ*, 299, 881

- Thuan, T. X. 1991, in *Massive Stars in Starburst*. In: Leitherer C., Walborn N. R., Heckman T. M., Norman C. A. (eds). Cambridge: Cambridge University Press, p. 183
- Thuan, T. X., Izotov, Y. I., & Lipovetsky, V. A. 1995, *ApJ*, 445, 108
- Trujillo, I., Graham, A. W., & Caon, N. 2001, *MNRAS*, 326, 869
- Vanzi, L., Rieke, G. H., Martin, C. L., & Shields, J. C. 1996, *ApJ*, 466, 150
- Vanzi, L., Hunt, L. K., & Thuan, T. X. 2002, *A&A*, 390, 481
- Vazdekis, A., Casuso, E., Peletier, R. F., & Beckman, J. E. 1996, *ApJS*, 106, 307
- Vorontsov-Vel'Yaminov, B. A. 1977, *A&AS*, 28, 1
- Wainscoat, R. J. & Cowie, L. L. 1992, *AJ*, 103, 332
- Whitmore, B. C., Lucas, R. A., McElroy, D. B., Steiman-Cameron, T. Y., Sackett, P. D., & Olling, R. P. 1990, *AJ*, 100, 1489
- Young, C. K. & Currie, M. J. 1994, *MNRAS*, 268, L11



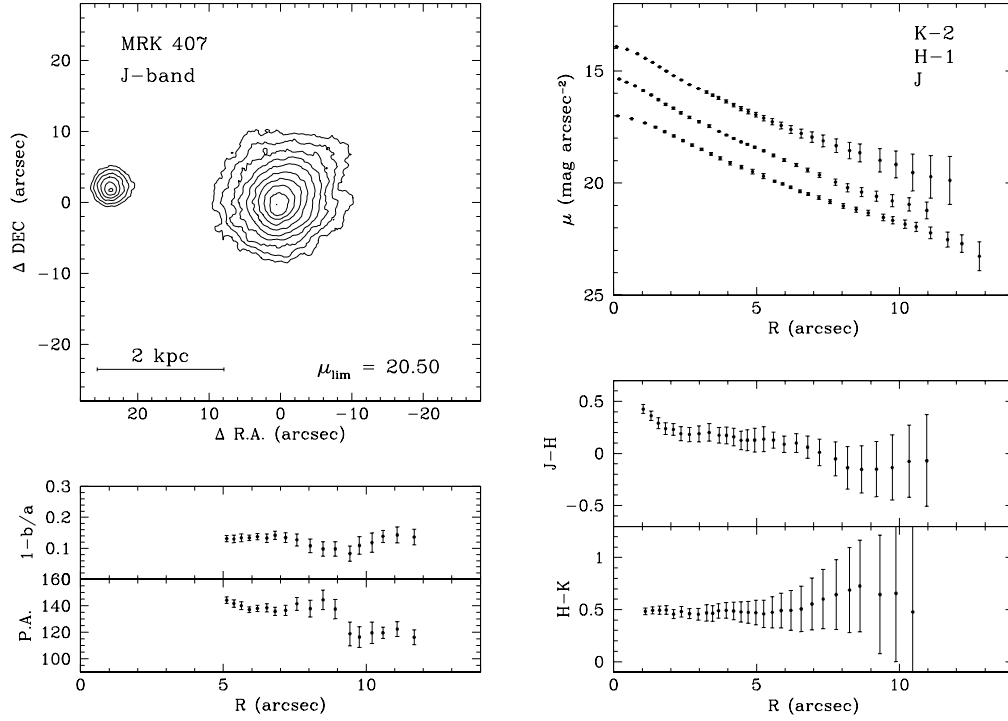


Fig. 1.— Top-left panel: Contour map of the galaxy. The contours are spaced by 0.5 mag. The surface brightness level corresponding to the outermost contour and the spatial scale are shown in each panel. North is up and East to the left. Top-right panel: Surface brightness profiles;  $R$  is the equivalent radius. Bottom-left panel: Position angle and ellipticity profiles (empty circles mean that the ellipse fitting algorithm fails to compute the isophote’s P.A. and ellipticity, and adopts instead the last measured value). Bottom-right panel: Color profiles.

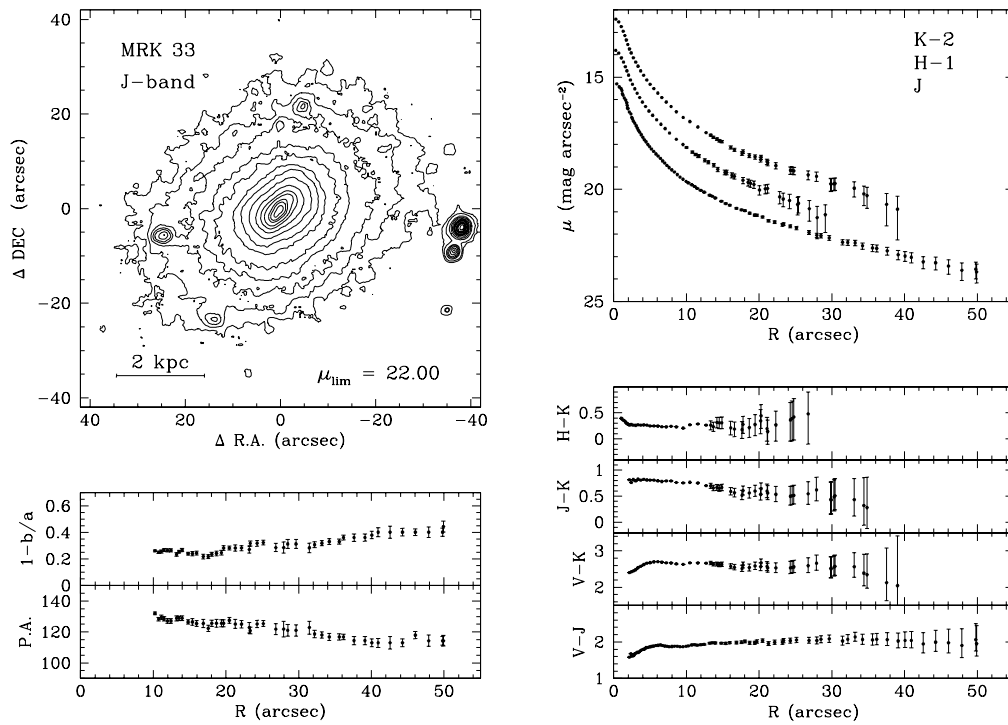


Fig. 1.— Continued

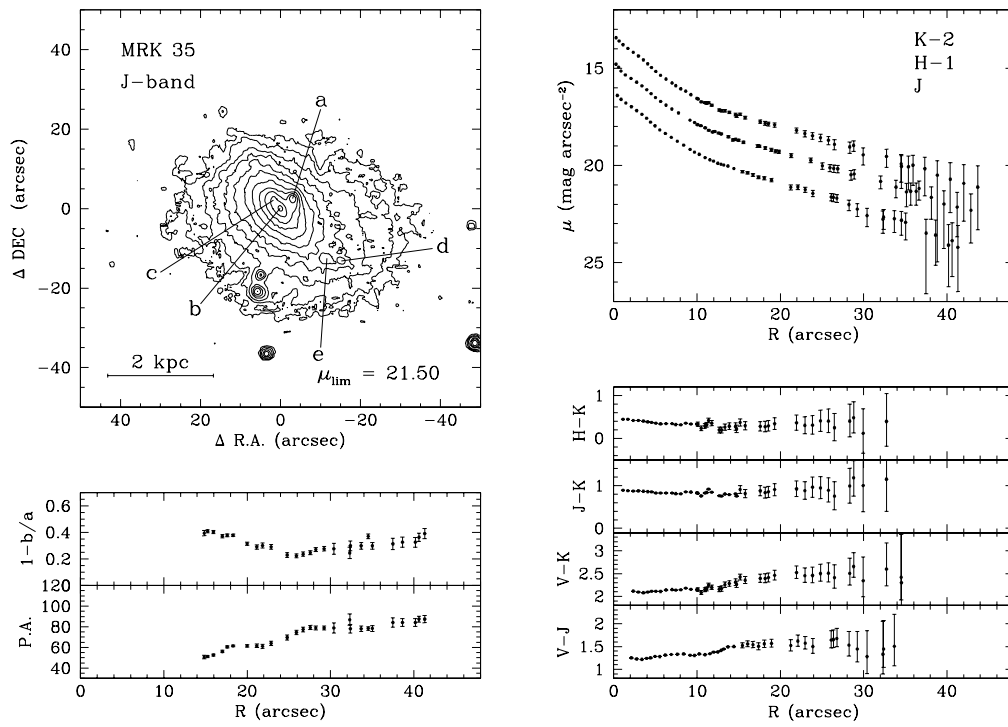


Fig. 1.— Continued

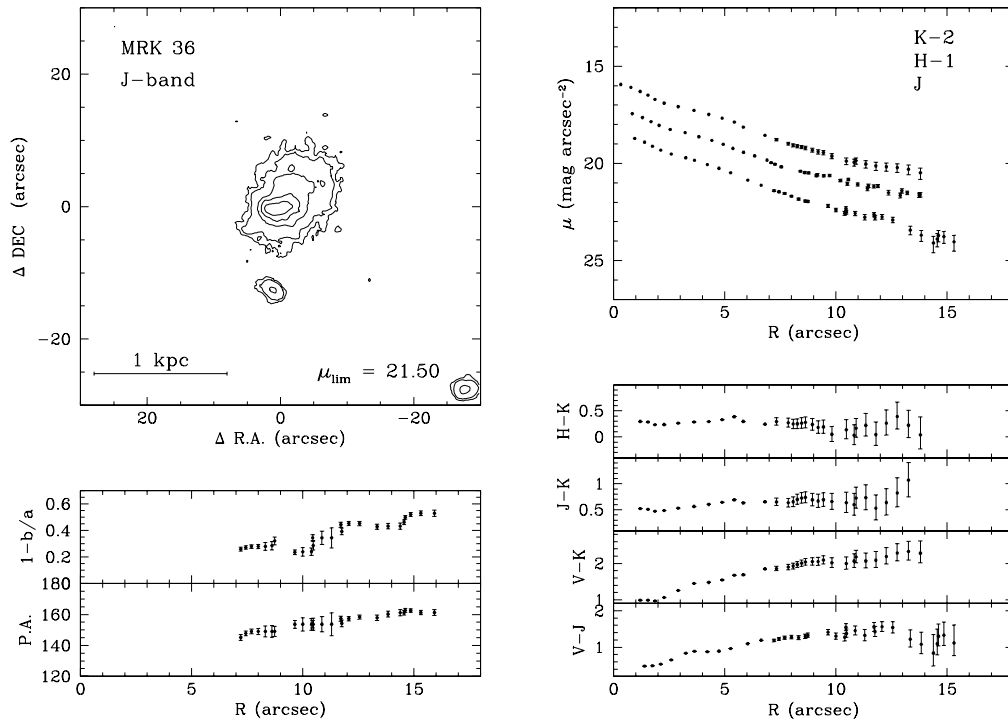


Fig. 1.— Continued

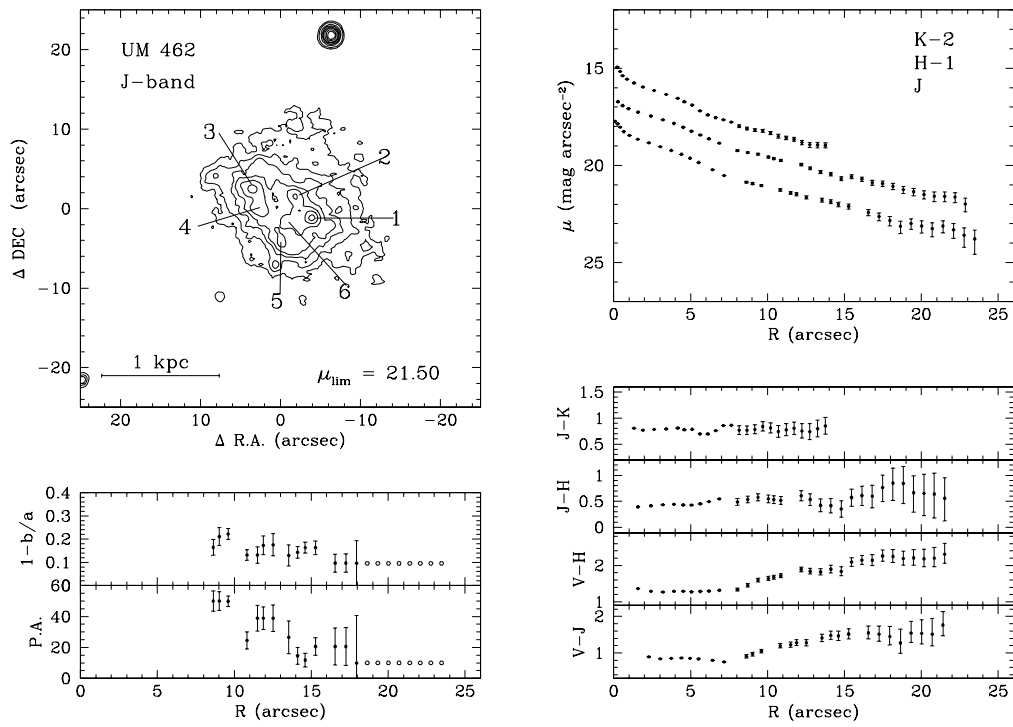


Fig. 1.— Continued

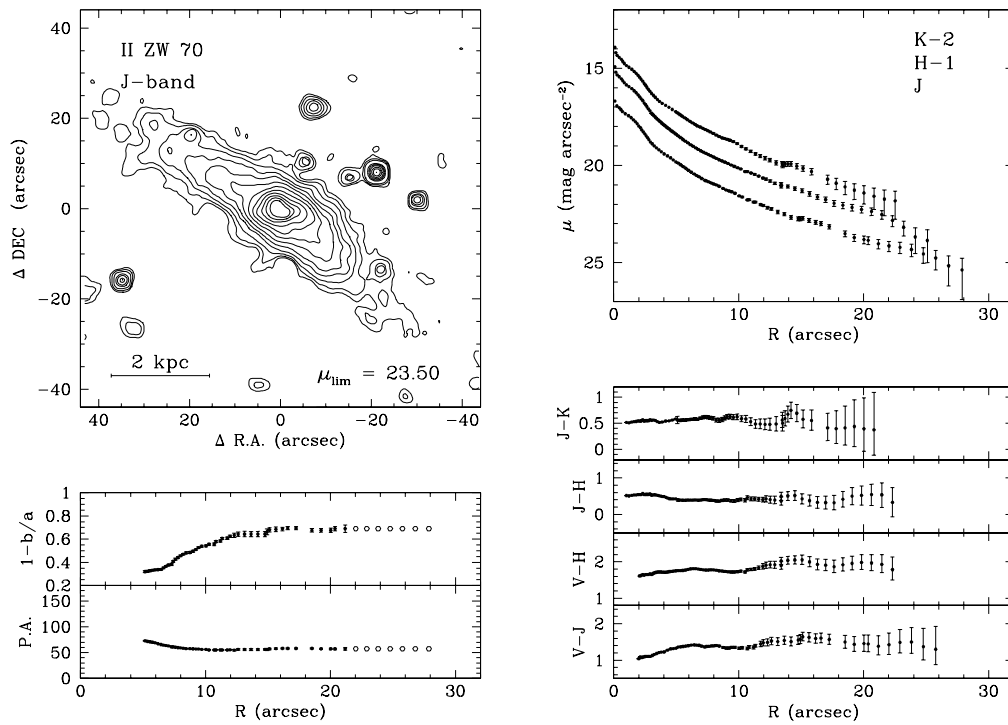


Fig. 1.— Continued

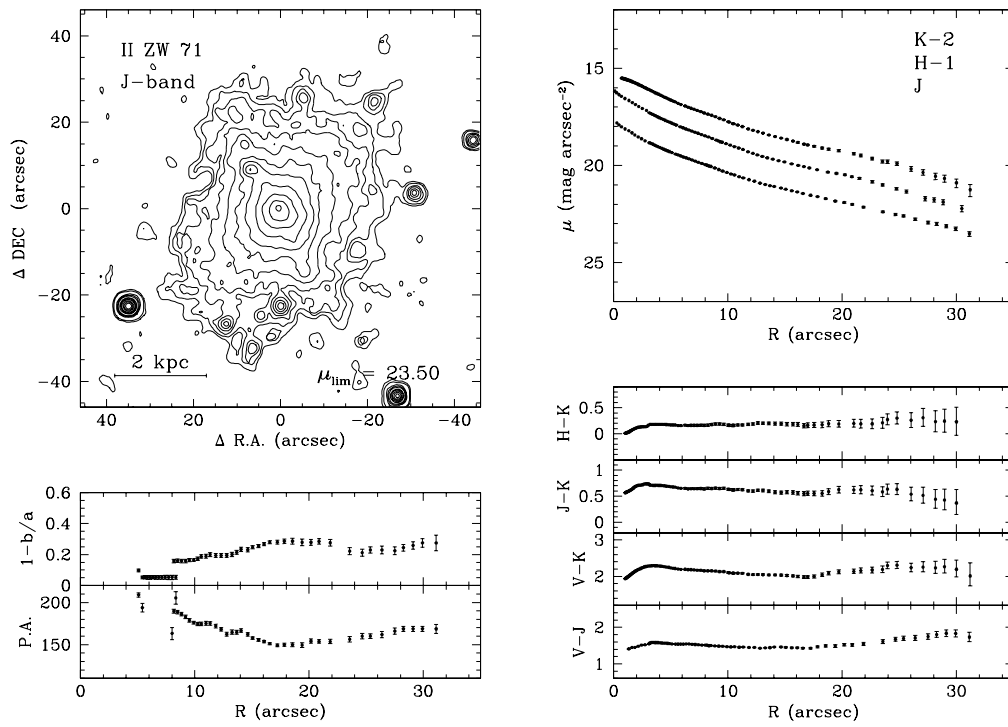


Fig. 1.— Continued

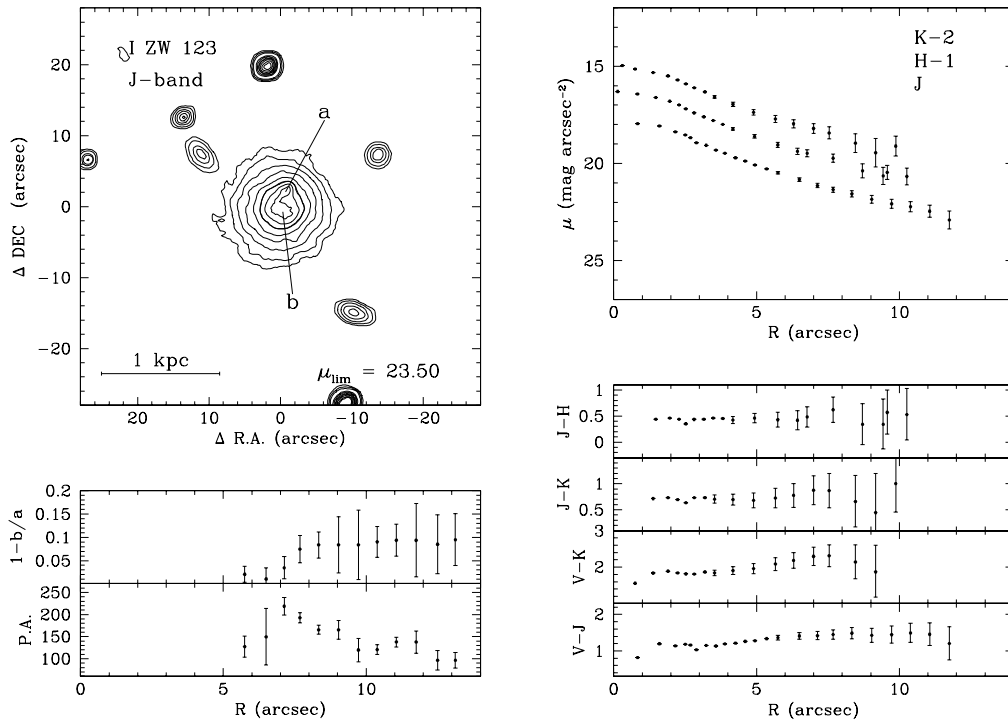


Fig. 1.— Continued



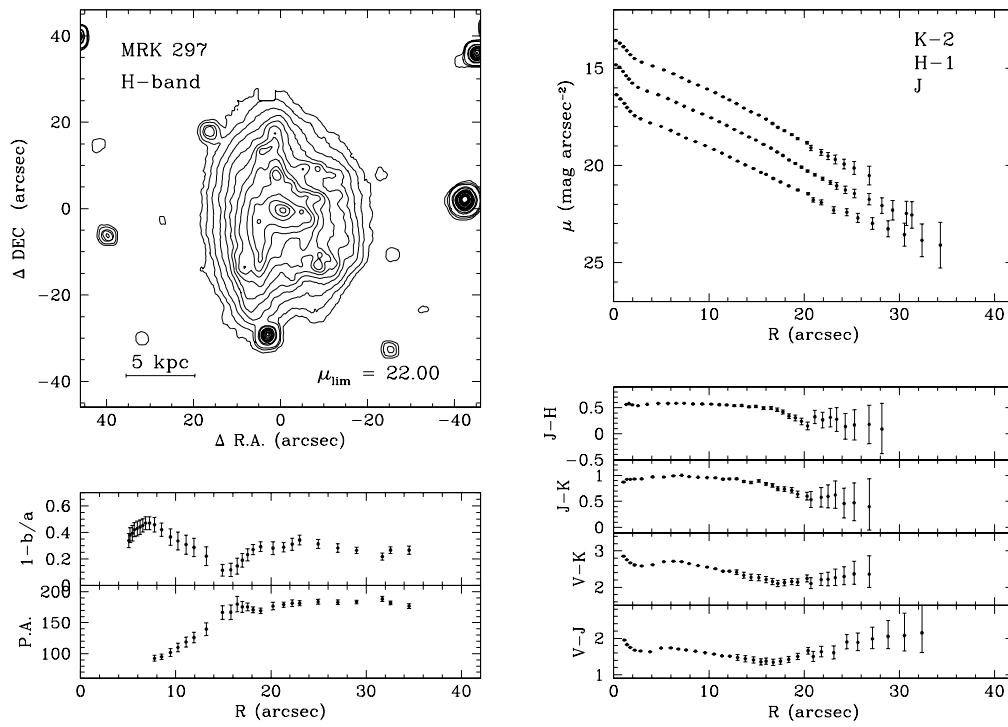


Fig. 1.— Continued

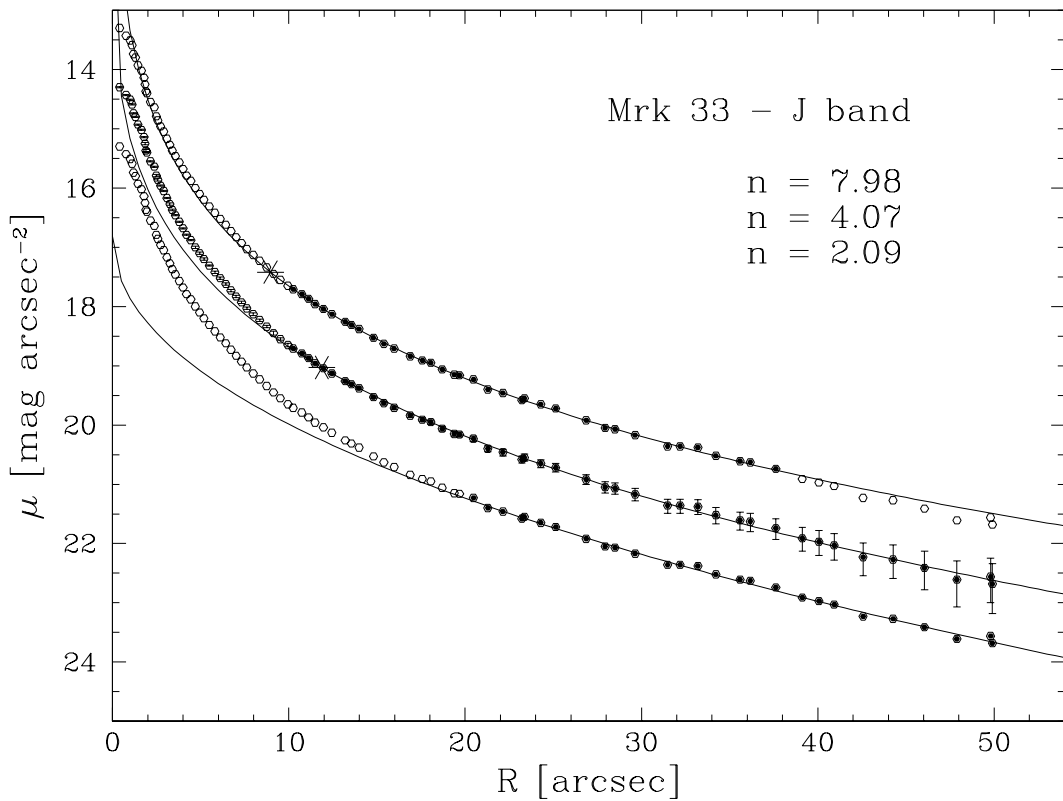


Fig. 2.— Three examples of a Sérsic fit to the  $J$ -band light profile of Mrk 33 are shown. Filled symbols identify the radial interval over which the profile was fitted; stars mark the effective radius and effective surface brightness. The middle profile is shifted up by 1 mag, the upper profile by 2 mags. Notice how all fits appear to be equally good (rms is  $\lesssim 0.04$  mags). See text and Table 4 for further details.

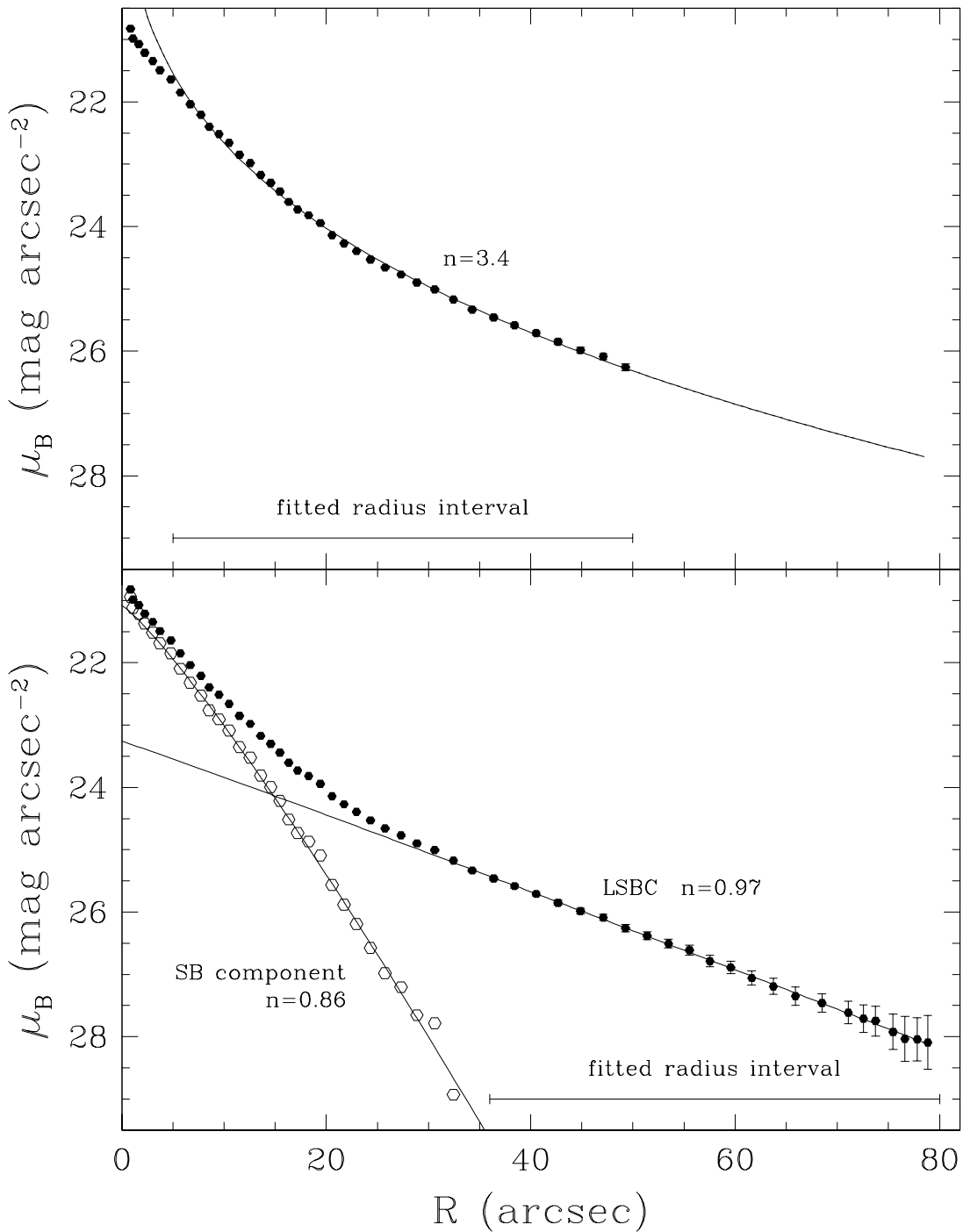


Fig. 3.— Upper panel: the  $B$ -band light profile of VII Zw 403, plotted down to  $\mu_B \simeq 26.3\text{mag}/\square''$ , shows a relatively smooth curvature, and can be best fit, in the range  $5'' < R < 50''$ , by a Sérsic law with  $n = 3.40$ . Lower panel: A deeper light profile, reaching down to  $\mu_B \simeq 28.5\text{mag}/\square''$ , is decomposed into a Sérsic law (LSBC) and a shallower Sérsic law (SB component).

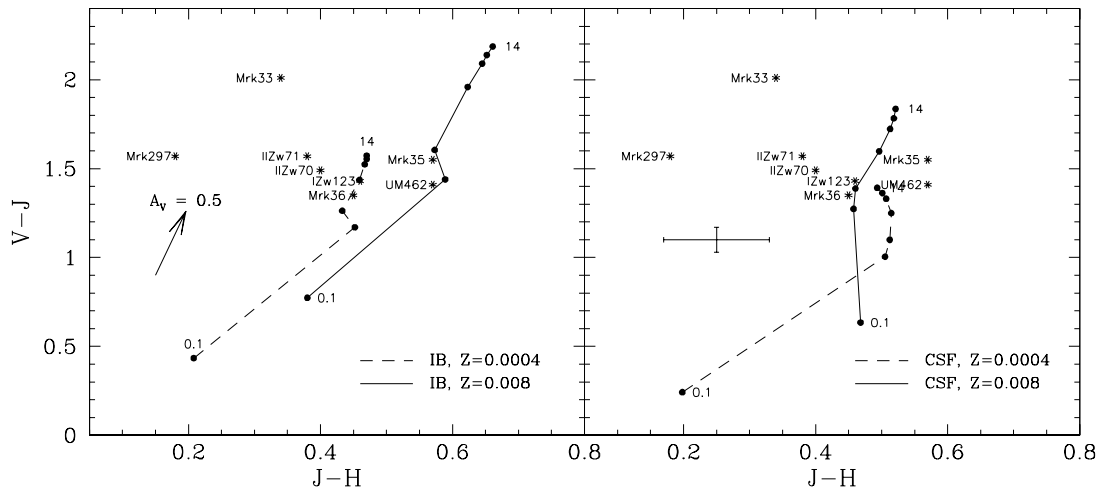


Fig. 4.—  $V-J$  vs  $J-H$  diagram for the LSBC of the sample galaxies. We also plot the evolutionary tracks of metallicity  $z = 0.0004$  and  $z = 0.008$  for an instantaneous burst (IB, left panel) and for continuous star formation (CFS, right panel). The arrow in the left panel indicates the shift in the plot due to an extinction of 0.5 V magnitudes, while the cross in the right panel shows the typical uncertainty.

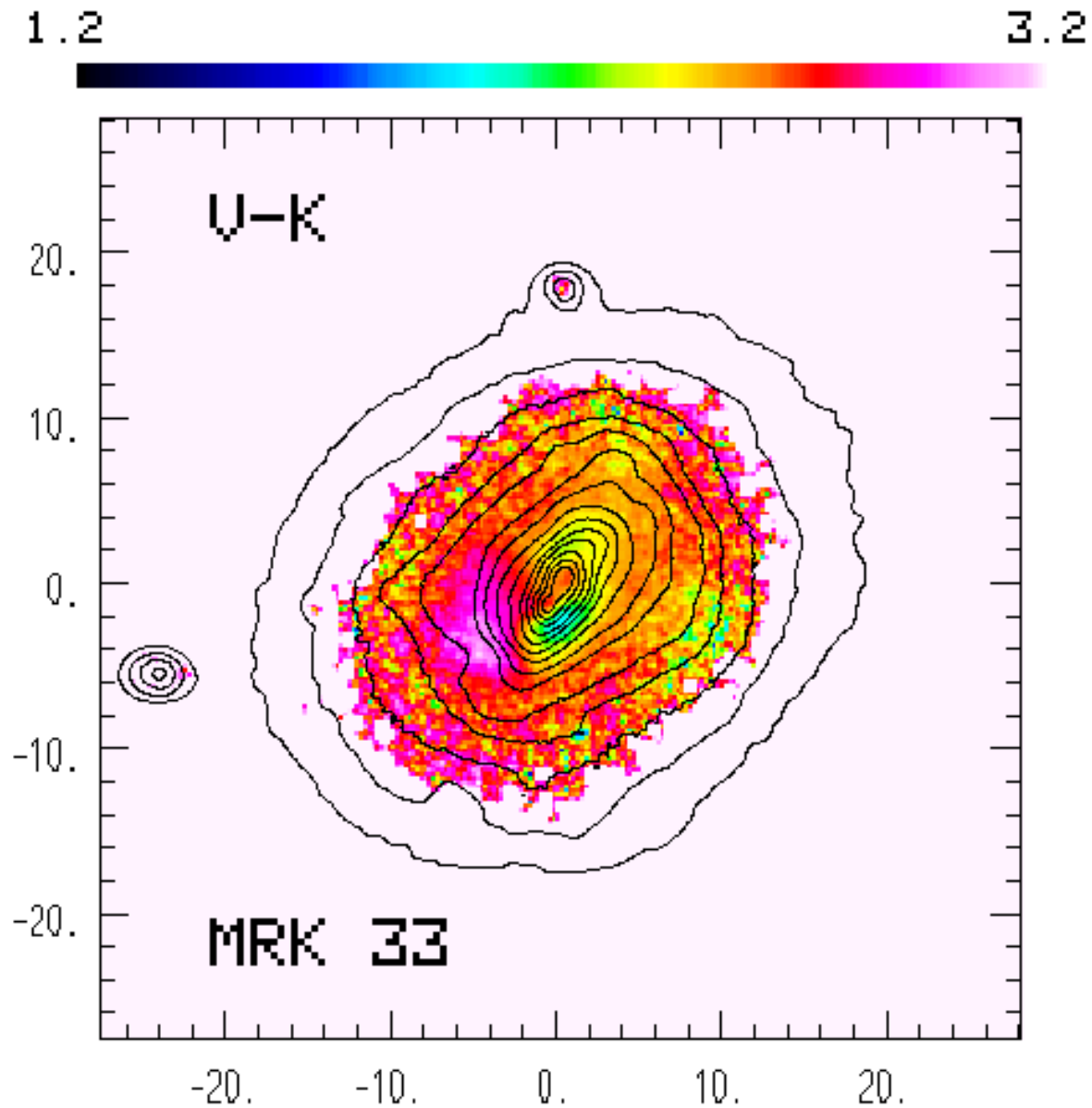


Fig. 5.—  $V-K$  color map of Mrk 33 overlaid with the  $B$ -band isophotes. The linear color scale is shown in the panel. North is to the top and east is to the left. Axis units are in arcseconds. The lowest isophote level is  $\mu_B = 23.5 \text{ mag arcsec}^{-2}$ ; isophotes are spaced 0.5 mag apart.

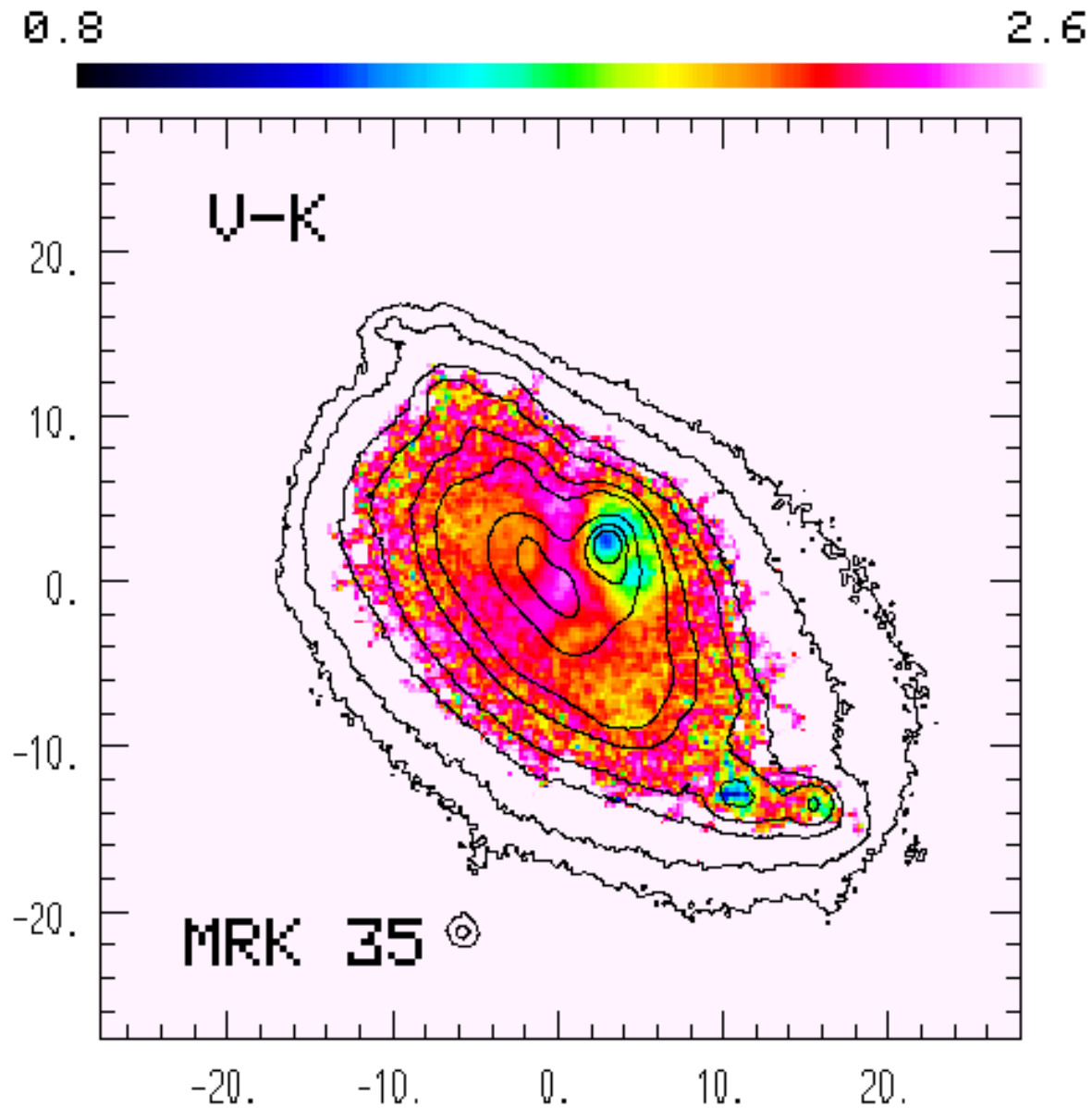


Fig. 6.—  $V-K$  color map of Mrk 35 overlaid with the  $B$ -band isophotes. The linear color scale is shown in the panel. North is to the top and east is to the left. Axis units are in arcseconds. The lowest isophote level is  $\mu_B = 23.0 \text{ mag arcsec}^{-2}$ ; isophotes are spaced 0.5 mag apart.

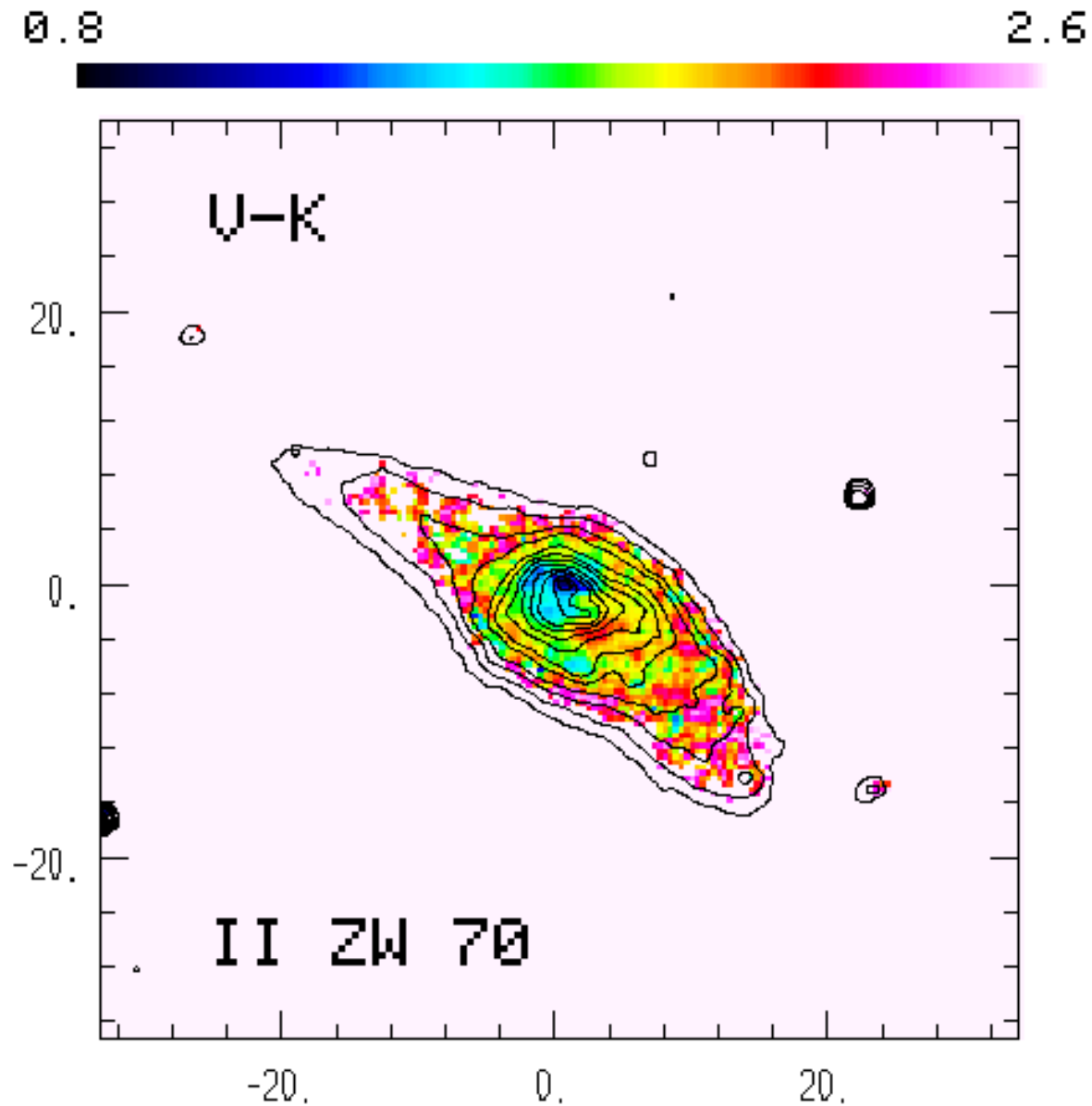


Fig. 7.—  $V-K$  color map of II Zw 70 overlaid with the  $V$ -band isophotes. The linear color scale is shown in the panel. North is to the top and east is to the left. Axis units are in arcseconds. The lowest isophote level is  $\mu_V = 23.5 \text{ mag arcsec}^{-2}$ ; isophotes are spaced 0.5 mag apart.

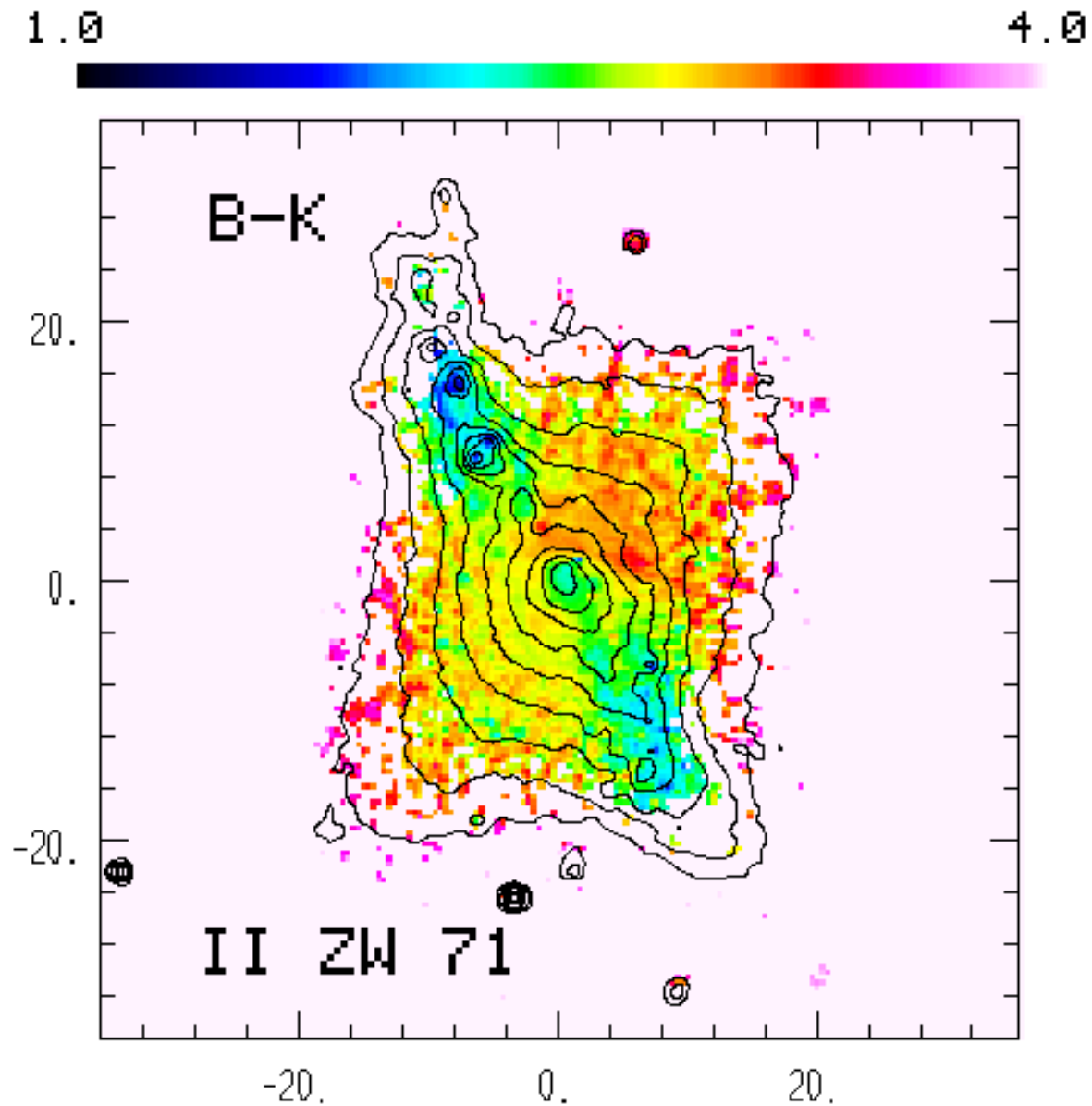


Fig. 8.—  $B-K$  color map of II Zw 71 overlaid with the  $B$ -band isophotes. The linear color scale is shown in the panel. North is to the top and east is to the left. Axis units are in arcseconds. The lowest isophote level is  $\mu_B = 24.0 \text{ mag arcsec}^{-2}$ ; isophotes are spaced 0.5 mag apart.



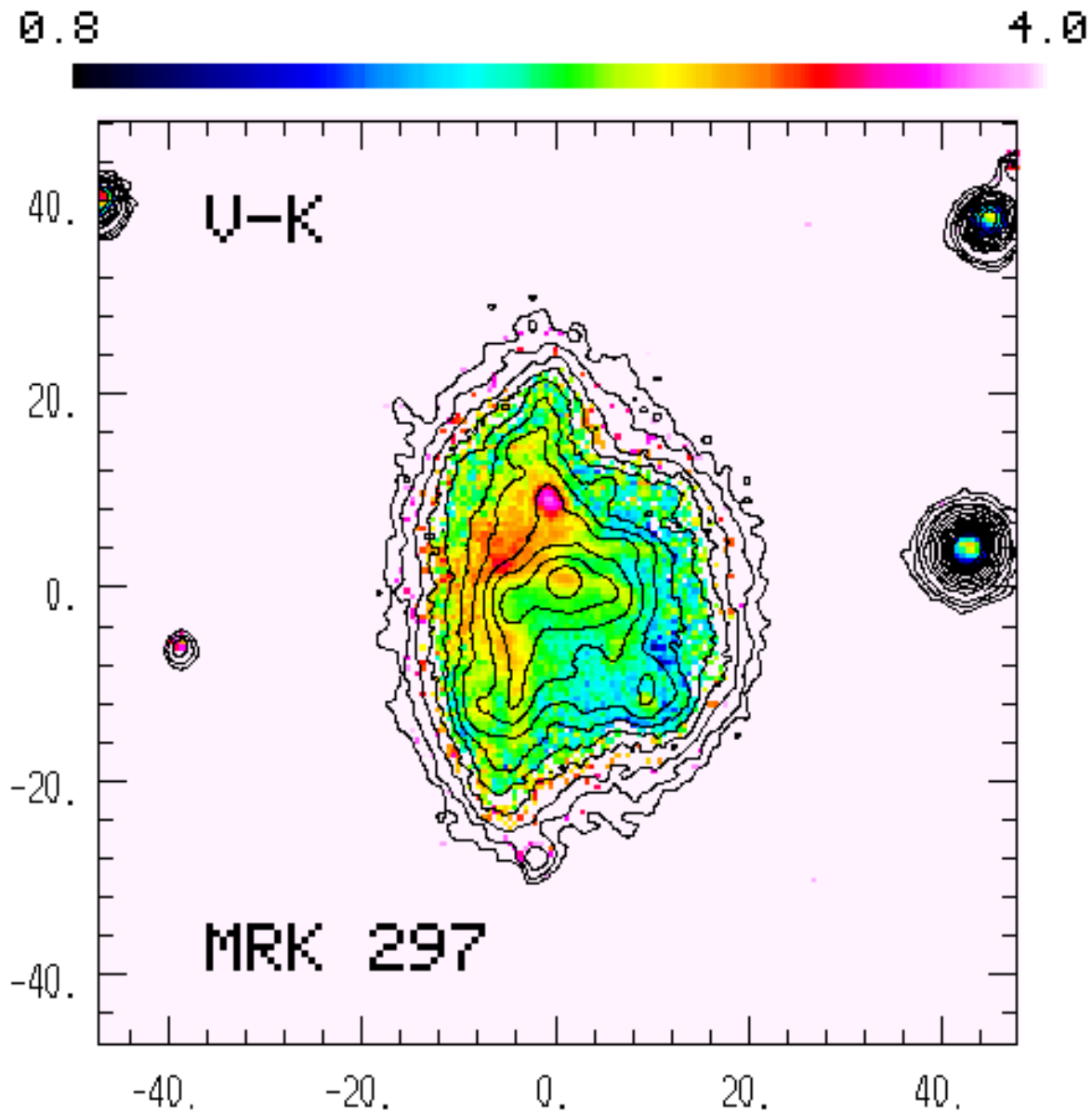


Fig. 9.—  $V-K$  color map of Mrk 297 overlaid with the  $V$ -band isophotes. The linear color scale is shown in the panel. North is to the top and east is to the left. Axis units are in arcseconds. The lowest isophote level is  $\mu_V = 24 \text{ mag arcsec}^{-2}$ ; isophotes are spaced 0.5 mag apart.